

Filamentary Molecular Cloud Formation via Collision-induced Magnetic Reconnection in Cold Neutral Medium

SHUO KONG (孔朔),¹ ROWAN J. SMITH,² DAVID WHITWORTH,³ AND ERIKA T. HAMDEN¹

¹*Steward Observatory, University of Arizona, Tucson, AZ 85719, USA*

²*SUPA, School of Physics and Astronomy, University of St Andrews, North Haugh, St Andrews, KY16 9SS*

³*Universidad Nacional Autónoma de México, Instituto de Radioastronomía y Astrofísica, Antigua Carretera a Pátzcuaro 8701, Ex-Hda.*

San José de la Huerta, 58089 Morelia, Michoacán, México

ABSTRACT

We have investigated the possibility of molecular cloud formation via the Collision-induced Magnetic Reconnection (CMR) mechanism of the cold neutral medium (CNM). Two atomic gas clouds with conditions typical of the CNM were set to collide at the interface of reverse magnetic fields. The cloud-cloud collision triggered magnetic reconnection and produced a giant 20 pc filamentary structure which was not seen in the control models without CMR. The cloud, with rich fiber-like sub-structures, developed a fully molecular spine at 5 Myr. Radiative transfer modeling of dust emission at far infrared wavelengths showed that the middle part of the filament contained dense cores over a span of 5 pc. Some of the cores were actively forming stars and typically exhibited both connecting fibers in dust emission and high-velocity gas in CO line emission, indicative of active accretion through streamers. Supersonic turbulence was present in and around the CMR-filament due to inflowing gas moving at supersonic velocities in the collision mid-plane. The shocked gas was condensed and transported to the main filament piece by piece by reconnected fields, making the filament and star formation a bottom-up process. Instead of forming a gravitationally bounded cloud which then fragments hierarchically (top-down) and forms stars, the CMR process creates dense gas pieces and magnetically transports them to the central axis to constitute the filament. Since no turbulence is manually driven, our results suggest that CMR is capable of self-generating turbulence. Finally, the resulting helical field should show field-reversal on both sides of the filament from most viewing angles.

Keywords: Molecular clouds; Magnetic fields; Star formation

1. INTRODUCTION

The formation and evolution of filamentary molecular clouds are crucial for our understanding of star formation and the evolution of the interstellar medium in galaxies (Hacar et al. 2023). To put it simply, gas in the interstellar medium (ISM) contracts to form clouds when

it becomes self-gravitating, which could be triggered by mechanisms such as colliding flows and gravitational instability (see Chevance et al. 2023, and references therein). During this process gas may begin as cold neutral medium (CNM) and transition to molecular while getting denser.

Observations have told us that a significant number of clouds show a prominent filamentary structure, e.g., the Orion A cloud as a whole (Polychroni et al. 2013; Stutz & Kainulainen 2015), the L1495 filament in the Taurus cloud (Li & Goldsmith 2012; Palmeirim et al. 2013; Shimajiri et al. 2019), and the California cloud as a whole (Lada et al. 2009; Lewis et al. 2021). Several models for filament formation have been proposed. For instance, the collapse of an initially asymmetric sheet can produce a filamentary structure (Burkert & Hartmann 2004). Supersonic turbulence can create shocked layers which may evolve into filaments (Li & Nakamura 2004), but these filaments should be stochastically distributed unless a significant source of anisotropy is present. Note, here we are referring to local mechanisms that produce filaments that may or may not be parallel to the Galactic plane. Large-scale filamentary clouds that are triggered by spiral potentials in the Galactic disk are out of the scope of this work (but see, for example, Smith et al. 2020).

Helical magnetic fields provide a cylindrical symmetry that can hold a filamentary structure, making it possible to have isolated large filamentary clouds. For instance, Heiles (1997) showed a large-scale line-of-sight reverse magnetic field around the famous Orion A giant molecular cloud. While Heiles (1997); Tahani et al. (2019) favored a bow-shape field, Poidevin et al. (2011) instead inferred a helical field wrapping the OMC-1 filament. Theoretically, Fiege & Pudritz (2000) showed in their model that a helical field stabilizes a cylindrical cloud. However, such a field configuration was not previously seen in numerical simulations (see, however, a recent work by Zhao et al. 2024).

In an effort to explain a peculiar observational feature in the Stick filament in the Orion A cloud, Kong et al. (2021, hereafter K21) proposed a collision-induced magnetic reconnection

(CMR) mechanism that was able to form a single filament with helical fields. Their model incorporated a field reversal pattern into the initial conditions (motivated by the Heiles observation in Orion) and successfully reproduced the observed morphology, density distribution, and kinematics of the Stick. Field-reversals are also observed around other filamentary clouds, including the Perseus cloud and the California cloud (Tahani et al. 2018, 2022). In the Galactic disk, we know there are large-scale field-reversals (Han et al. 2018). Any gas motion that brings together the reverse field can trigger CMR, even if the field is not exactly anti-aligned (see Figures 26, 27 in Kong et al. 2021).

The helical field, which was a natural result of CMR, created and maintained the filament with relatively strong magnetic surface pressure. It showed that magnetic fields can actively produce dense gas, unlike the stereotype in which magnetic fields only passively hinder gas concentration. Later, Kong et al. (2022, hereafter K22) showed that a CMR-filament like the Stick would collapse along its major axis and form a star cluster. However, the star formation rate was relatively low due to the surface field that hindered gas accretion (which was only possible through streamers).

If one sub-filament in the Orion A cloud is explicable by CMR, then the natural follow-up question is whether the entire Orion A formed in a similar fashion. In this paper, we follow up K22 with a pilot investigation of the formation of a filamentary molecular cloud via CMR in the cold neutral medium (CNM) rather than molecular gas. Specifically, we aim to study the formation of a 10-pc-scale filamentary cloud from CNM. The goal is to see if CMR has the potential to form a long molecular filament like the Orion A. For example, is it able to form a filament 10 times longer by simply scaling up the initial sizes in K22? Does it produce fibers as seen in observations (e.g., Hacar et al. 2018)?

Is it capable of generating turbulence? Most importantly, can CMR convert CNM to molecular gas? At this point, we do not intend to reproduce any specific cloud, but using Orion A as a guide for our exploration. If the answer to the above questions is yes, meaning the potential is there, then we can attempt to scale the initial conditions accordingly to reproduce key features for specific clouds. For example, although the CMR model in this paper does not match the high column density of Orion A, we can increase the initial density to produce a filament with higher densities. Although we are forming a 10-pc filament, we can increase the initial scales to produce a 100-pc filament just like Orion A (Großschedl et al. 2018).

In reality, the initial condition might not be the collision between two spherical clouds. It could be the expansion of a bubble that hits a wall of gas with reverse fields. The bubble and the wall could have multiple pairs of clumps that collide and trigger CMR, thus forming a number of sub-filaments that as a whole resemble a large filament. Nonetheless, the exploration in this paper provides a useful initial look into the capability of CMR and points us to the right direction in terms of modeling observed filaments.

Although the original model of CMR in K21 started with fully molecular conditions, the very beginning of a giant molecular cloud is likely CNM, if not warm neutral medium (WNM). Observationally, this conjecture relies on the fact that we have not clearly seen large-scale colliding molecular gas on either side of the Orion A filament (e.g., Kong et al. 2018). On the other hand, there are narrow velocity components of HI gas around Orion A that appear to be CNM (Soler et al. 2018). Such an origin appears feasible and theoretically, CNM is the precursor of molecular gas. Therefore, in this paper, we model the formation of a molecular filament via CMR in CNM. We will examine the

mentioned properties, including the molecular fraction, the sub-structures of the filament, and (supersonic) turbulence.

In the following, we first briefly introduce our simulation setup in §2. Then, we report our findings in the results section §3. We discuss the implications based on the results in §4. Finally, we summarize our findings and conclude in §5.

2. MODEL SETUP

Following K22, we use a modified version of the AREPO code (Springel 2010) to simulate CMR. The code configuration is the same as K22, including magnetohydrodynamics (MHD, Pakmor et al. 2011), gravity (Springel 2005), time-dependent chemistry (Gong et al. 2017; Clark et al. 2019) including gas self-shielding (Clark et al. 2012a) from an ambient interstellar radiation field, heating/cooling processes (Clark et al. 2019), and sink particles to represent sites of star formation (Bate et al. 1995; Greif et al. 2011; Tress et al. 2020). A refinement that ensures the Jeans scale be resolved by at least 16 cells is adopted (Truelove et al. 1997). See K22 method section for details.

Here we will use as an initial condition a simple toy model of two colliding spherical clouds. Figure 1 shows the initial conditions for the fiducial model. Hereafter we name the fiducial model MRCOLA_CNM (as opposed to the fiducial model MRCOLA in K22). The initial condition for MRCOLA_CNM is structurally the same as MRCOLA in that two spherical clouds are embedded in a less dense medium and collide at the interface of anti-parallel (reverse) magnetic fields. Unlike in K22, here the colliding clouds are CNM that is embedded in WNM. Accordingly, the initial gas composition is fully atomic instead of molecular. The elemental abundances are the same as those in K22 and correspond to solar values. Since we are modeling the scale of 10 pc, we enlarge simulation scales by a factor of 10 (compared to K22). Specifically, the colliding clouds now have radii

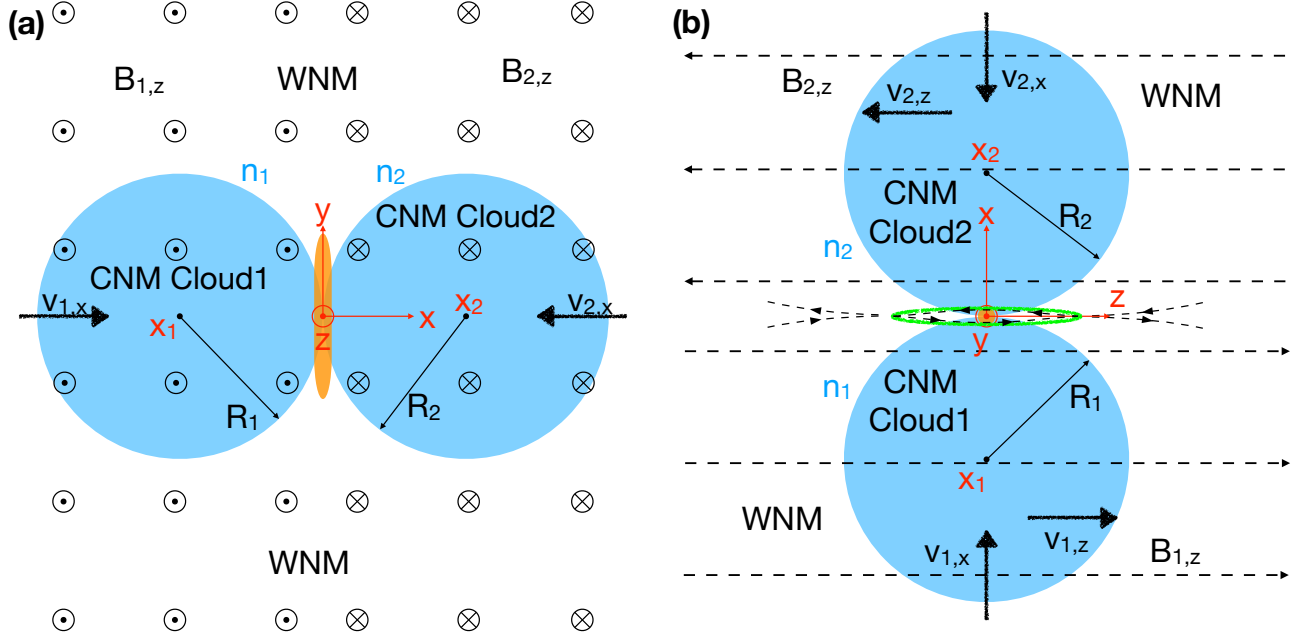


Figure 1. MRCOLA_CNM initial condition in two viewing angles. **(a):** A view in the x - y plane. Two spherical CNM clouds are in thermal pressure balance with the ambient WNM. They collide at the origin of the Cartesian coordinate system (red) in which the z -axis points toward us (red circle-point, right-hand rule). The colliding velocities are $v_{1,x}$ and $v_{2,x}$ for the two clouds, respectively. Magnetic fields point toward us (black circle-points) for $x < 0$ and away from us (black circle-crosses) for $x > 0$. The collision triggers the formation of the *filament* (orange) along the y -axis. Note the *filament* is imaginary in this initial condition figure. It will form after the cloud collision. **(b):** A view in the z - x plane. In this view, magnetic fields are parallel to the plane of the sky. The y -axis points toward us (red circle-point) so we see the *filament* (orange) cross-section (again imaginary). The green ellipse marks the location of the compression *pancake* if no magnetic fields. With CMR, the field reconnects at two edges of the *pancake* and forms a *field-loop* (black dashed arrow-curve inside the green ellipse) around the *pancake*. The magnetic tension squeezes the *pancake* to the central axis (y -axis), making it a *filament*. Outside the *pancake*, the reconnected field forms two half loops and pulls gas away.

of 9 pc and the domain has a size of 80 pc. The relatively large domain size is to avoid boundary artifacts.

For the clouds, we adopt typical physical properties for the CNM, i.e., a total H number density 30 cm^{-3} and a gas kinetic temperature $T_{\text{CNM}} = 100 \text{ K}$. For the ambient gas, we adopt typical properties for WNM, i.e., $n_{\text{WNM}} = 0.5 \text{ cm}^{-3}$ and $T_{\text{WNM}} = 6000 \text{ K}$, so that it is in thermal pressure balance with the clouds. Each CNM cloud has a total mass of $\sim 3000 M_{\odot}$. The WNM total mass is ~ 3 times the CNM total mass. The relative collision speed ($\sim 5 \text{ km s}^{-1}$) considers the typical relative speed between multiple line components toward inter-

stellar clouds. For instance, the HI observation by Heiles (1997) showed multiple HI components around Orion A with $\sim 5\text{--}10 \text{ km s}^{-1}$ separations. Around the Taurus B213 filament, Shimajiri et al. (2019) showed a similar separation between HI components and a few km s^{-1} separation in molecular gas emission. We thus set the speed for each colliding CNM cloud to 2.5 km s^{-1} . Unlike K22, we set the z -velocity to zero so the collision is head-on. Adding the shear velocity or an impact parameter will cause the rotation of the filament (see for example K22), which is not our focus in this paper. The magnetic field strength is set to $5 \mu\text{G}$ in each direction, simply following the HI Zeeman ob-

Table 1. Model Initial Conditions

Model	MRCOLA_CNM	MRCOLA_CNM_sameB	MRCOLA_CNM_noB
(1)	(2) fiducial	(3)	(4)
L	80 pc	80 pc	80 pc
T_{CNM}	100 K	100 K	100 K
T_{WNM}	6000 K	6000 K	6000 K
ζ	$3.0 \times 10^{-17} \text{ s}^{-1}$	$3.0 \times 10^{-17} \text{ s}^{-1}$	$3.0 \times 10^{-17} \text{ s}^{-1}$
ISRF	$1.7G_0$	$1.7G_0$	$1.7G_0$
n_{WNM}	0.5 cm^{-3}	0.5 cm^{-3}	0.5 cm^{-3}
n_1	30 cm^{-3}	30 cm^{-3}	30 cm^{-3}
R_1	9 pc	9 pc	9 pc
$v_{1,x}$	2.5 km s^{-1}	2.5 km s^{-1}	2.5 km s^{-1}
$v_{1,z}$	0	0	0
$B_{1,z}$	$5 \mu\text{G}$	$5 \mu\text{G}$	0
n_2	30 cm^{-3}	30 cm^{-3}	30 cm^{-3}
R_2	9 pc	9 pc	9 pc
$v_{2,x}$	-2.5 km s^{-1}	-2.5 km s^{-1}	-2.5 km s^{-1}
$v_{2,z}$	0	0	0
$B_{2,z}$	$-5 \mu\text{G}$	$5 \mu\text{G}$	0

NOTE—The physical quantities follow the notation in K22 Figure 1. L is the domain size. T_{CNM} is the initial temperature of the CNM clouds. T_{WNM} is the ambient WNM temperature. ζ is the cosmic-ray ionization rate. ISRF is in unit of Habing field G_0 . n_{WNM} is the ambient WNM number density. n_1 is the Cloud1 H number density. R_1 is the Cloud1 radius. $v_{1,x}$ is the Cloud1 collision velocity. $v_{1,z}$ is the Cloud1 shear velocity. $B_{1,z}$ is the B-field for $x < 0$. n_2 is the Cloud2 H number density. R_2 is the Cloud2 radius. $v_{2,x}$ is the Cloud2 collision velocity. $v_{2,z}$ is the Cloud2 shear velocity. $B_{2,z}$ is the B-field for $x > 0$.

servations in Heiles (1997). Table 1 column (2) lists the fiducial model parameters. The physical quantities follow the notation in Figure 1.

3. RESULTS AND ANALYSIS

In the following, we will be describing the physical process in a mostly qualitative way to show the physical picture. The goal is to test whether a molecular cloud can form from atomic gas (CNM) through the CMR process. We resort to future papers for detailed investigations of the various physical processes.

We define the nomenclature of a few most important objects during the CMR process. From now on, a *pancake* refers to the compressed cir-

cular structure between the colliding spheres. A *filament* refers to the main elongated structure formed along the y-axis. A *fiber* refers to the small wiggly structures in and around the filament. The *filament* can consist of numerous *fibers*. A *ring* refers to the circular and/or elliptic structure along the *filament*. A *fork* refers to the open tuning-fork-like structure at two ends of the *filament*. A *field-loop* refers to the magnetic field loop around the *pancake* after magnetic reconnection (the dashed loop around the *pancake* in Figure 1(b)). All other names not in the above nomenclature are considered temporary for description purpose.

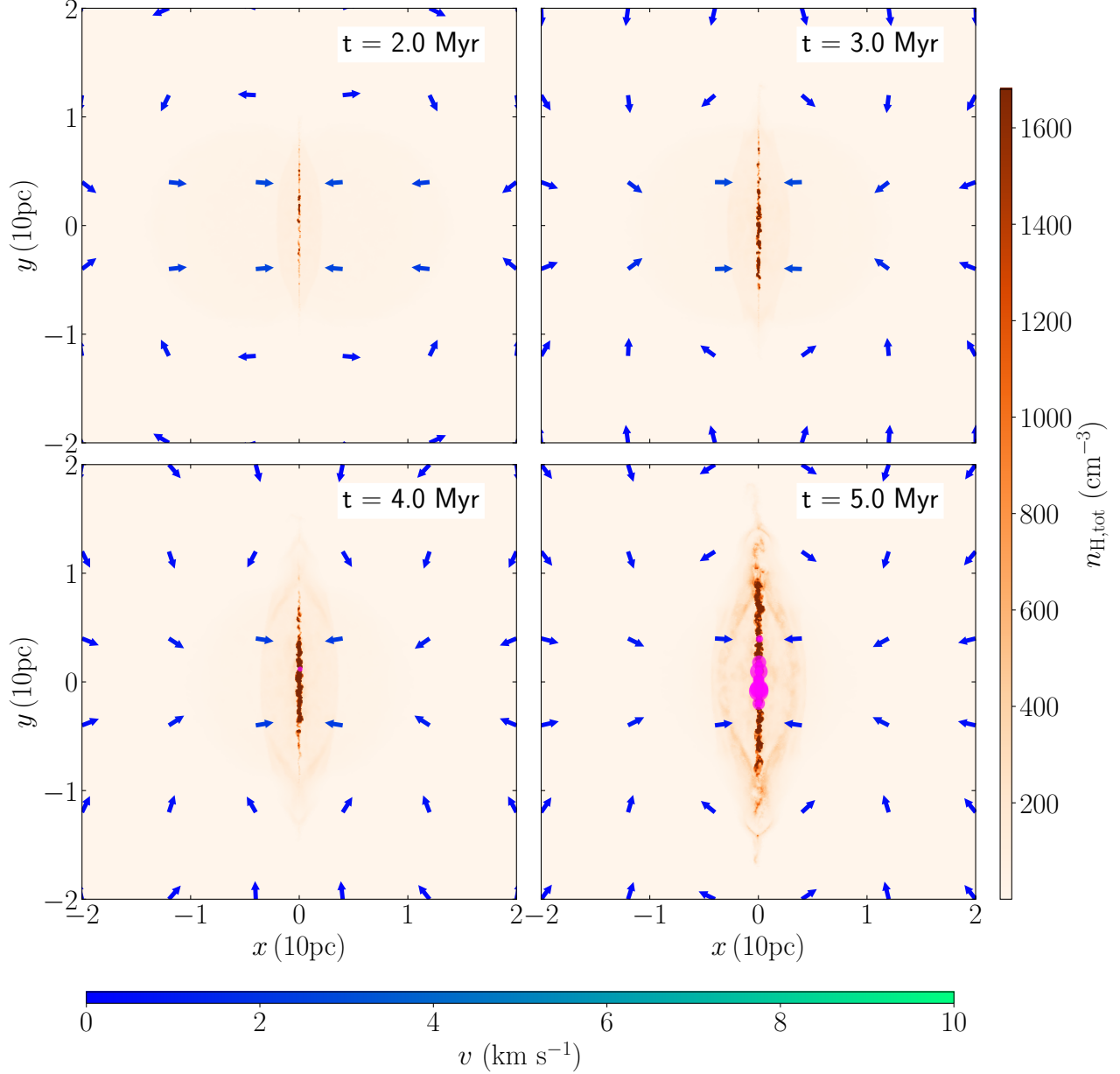


Figure 2. MRCOLA_CNM density slice plots for the $z=0$ plane. The linear color scale shows the total gas density in unit of $n_{\text{H,tot}}$. The magenta filled circles show the sinks. The circle size is proportional to the sink mass. The time step is shown at the top-right in each panel. The arrows show the velocity vectors. The arrow color scales with the velocity magnitude (the bottom color bar). This slice corresponds to Figure 1(a).

CMR is necessarily a 3D process with complex dynamics due to the interaction between gas and magnetic fields. To help readers better understand the process, we refer to a movie (file name `CMRfield.mp4`) in <https://doi.org/10.7910/DVN/CXHWRR> that shows the CMR process based on simulations from K21. The

movie shows the field lines and the gas rendering near the field-reversal plane (the $x=0$ plane in Figure 1). Our coordinate system is similar to their setup. In the movie, one can see the *pancake* initially which is later wrapped by *field-loops*, and the *filament* which is wrapped by helical fields at the end. The resulting field

around the filament is illustrated in Figure 2 of Kong et al. (2023).

3.1. Density Structures

Figure 2 shows density slice plots for $z=0$ plane. This plane corresponds to the setup as shown in Figure 1(a). Here, two spherical CNM clouds with a radius of 9 pc collide at $x=0$. Magnetic fields at $x<0$ point toward us and at $x>0$ point away from us. The $x=0$ plane is the field-reversal plane. Note, the spherical geometry is not a necessary requirement for CMR. Provided the colliding clouds have a protruding shape CMR-filament formation should be triggered (K21, Kong 2022).

Initially, the two CNM clouds move toward the $x=0$ plane. Once the collision happens, a dense gas layer forms in the collision mid-plane at $x=0$. The layer (not clear if it is a *filament* yet), marginally visible at $t=2$ Myr, gradually builds up high-density gas throughout the simulation. At the same time, the high pressure in the mid-plane expels gas in opposite directions along the y -axis, as indicated by the diverging arrows at $y \sim \pm 10$ pc. After ~ 4 Myr, sink formation begins. At $t=5$ Myr, the maximum sink mass reaches $16.5 M_{\odot}$. The sink has the potential of forming a massive star if the star formation efficiency $\gtrsim 50\%$ and only one star forms. From Figure 2 we can also see that the sink formation is along the dense layer. In total, there are 57 sinks at $t=5$ Myr and they concentrate in the middle part of the layer.

Figure 3 shows density slice plots for the $x=0$ plane. This is the collision mid-plane that shows up as the projected dense layer in Figure 2. We will see that the layer indeed becomes a *filament*. In this $x=0$ plane, the collision produces a dense *pancake* initially. The high pressure in this *pancake* drives material outward, which is indicated by the diverging velocity vectors at $y \sim \pm 10$ pc. Starting from $t=2$ Myr, converging movements in the *pancake* establish, which is indicated by the velocity vectors toward the

central axis. The approximately symmetric converging movements, which are more obvious from $t=3$ Myr, try to squeeze the *pancake* toward its central axis (the y -axis at $z=0$), while the bipolar outward movements at $y \sim \pm 10$ pc remain. Outside the *pancake* at $z \lesssim -10$ pc and $z \gtrsim 10$ pc, there is a strong outward movement along z -axis as indicated by the long diverging velocity vectors. Meanwhile, the *pancake* interior develops numerous *fibers* roughly parallel to the y -axis (mostly obvious at $t=2$ Myr).

As shown by K21 (e.g., their Figure 25), the above velocity patterns are typical results of CMR. The cloud collision triggers magnetic reconnection at the outer edges of the *pancake* ($z \sim \pm 7$ pc). The reconnected field forms *field-loops* around the *pancake* and half loops for $z < -7$ pc and $z > 7$ pc, which is illustrated in Figure 1(b). The *field-loops* pinch the *pancake* and make it a single *filament* along the y -axis. The converging velocity arrows in Figure 3 show the gas movement toward the *filament* due to the pinching. The half loops outside the *pancake* pulls gas away, resulting in the diverging velocity arrows along z -axis outside the *pancake*. The locations of the velocity reverse (e.g., $z \sim \pm 7$ pc at $t=1$ Myr) are the main CMR sites.

3.2. Kinematics

We examine the kinematics in the collision mid-plane and find that the gas velocity is sub-Alfvénic near the reconnection sites but super-Alfvénic in the *pancake*. The super-Alfvénic movement turns out to be supersonic. Figure 4 shows the sonic Mach number \mathcal{M} in the mid-plane where $\mathcal{M} \sim 1 - 8$ at $t=5$ Myr. Combining with Figure 3, we see that gas is transported to the central *filament* supersonically. In the innermost spine of the *filament*, the gas slows down to transonic to moderately supersonic ($\mathcal{M} \sim 2$) because it reaches stagnation (also see §3.4 and Figure 13). Note, the temperature in the spine is as low as ~ 5 K. Nevertheless, the supersonic transportation in the

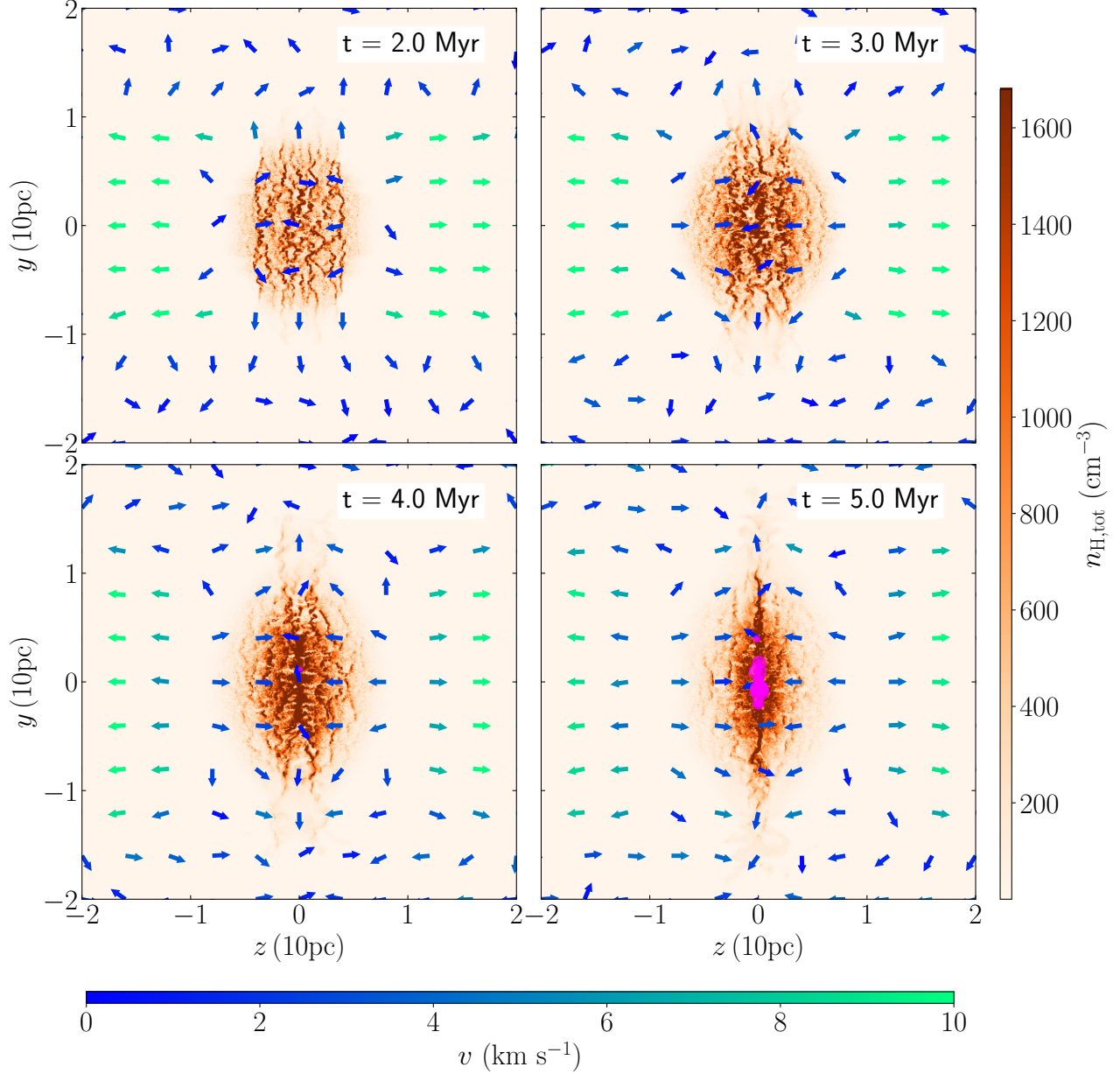


Figure 3. MRCOLA_CNM density slice plots for the collision mid-plane. It corresponds to the $x=0$ plane in Figure 1 and faces the positive x -direction. The linear color scale shows the total gas density in unit of $n_{\text{H,tot}}$. The magenta filled circles show the sinks. The circle size is proportional to the sink mass. The time step is shown at the top-right in each panel. The arrows show the velocity vectors. The arrow color scales with the velocity magnitude (the bottom color bar).

pancake results in supersonic turbulence in and around the *filament*. Note, there is no manually generated turbulence throughout the simulation. In other words, CMR self-generates supersonic turbulence as a result of the magnetic transportation of dense gas. As long as the collision persists, CMR continues to convert

colliding gas into dense gas in the collision mid-plane which is then transported to the *filament*, driving turbulence within the *filament*. CMR thus converts large-scale coherent motion (the laminar collision) to small-scale turbulence. A dedicated study of the nature of the turbulence will be carried out in the future, including the

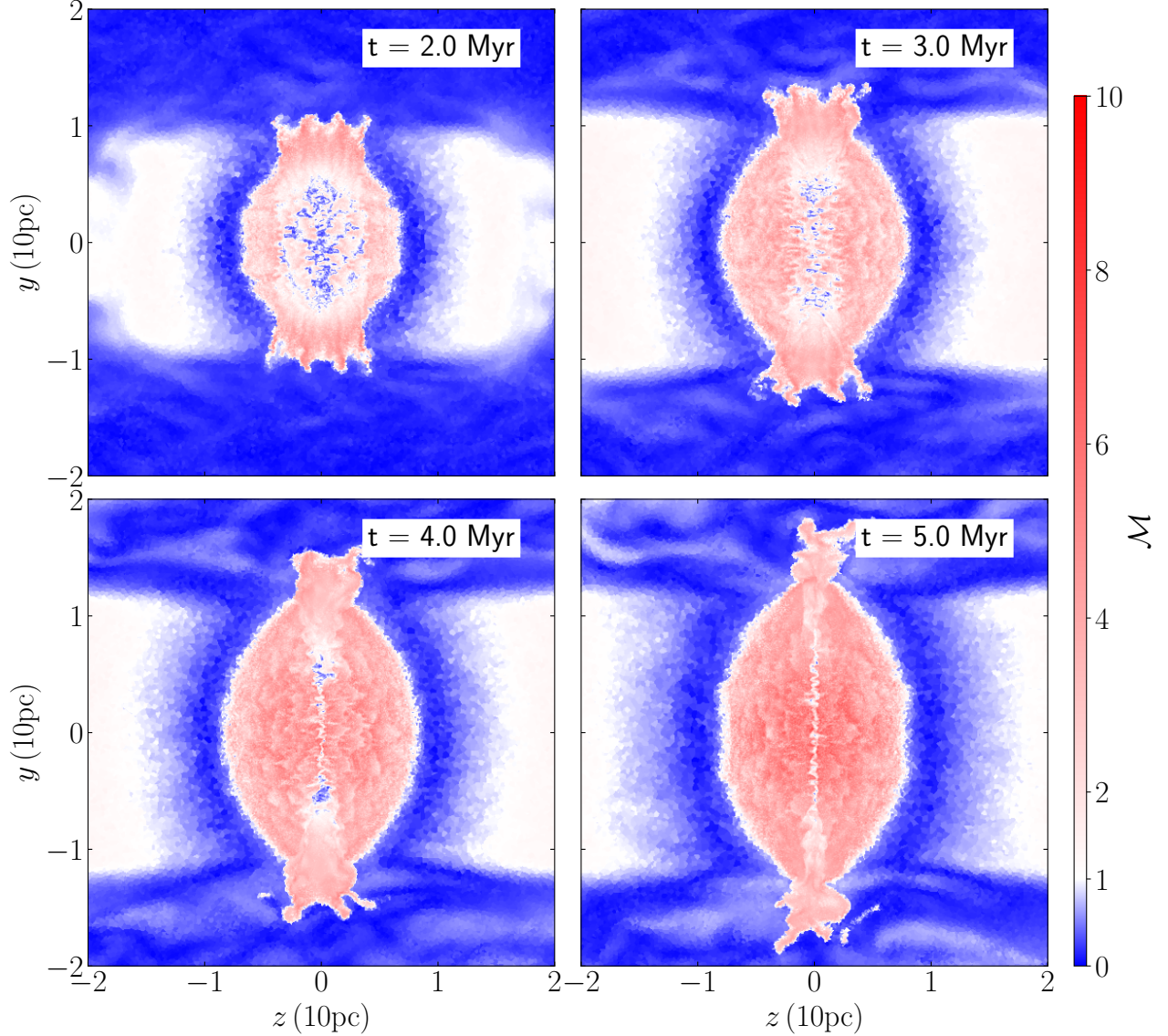


Figure 4. MRCOLA_CNМ sonic Mach number \mathcal{M} for the collision mid-plane ($x=0$). This is the same slice as Figure 3. The diverging color scheme diverges at $\mathcal{M} = 1$. The velocity direction can be depicted from Figure 3.

scale dependence and perhaps the power spectrum (in comparison with other models).

Meanwhile, the magnetic reconnection triggers plasmoid instability (see, for example, Bhattacharjee et al. 2009, and K21) in each z - x plane at the field-reversal interface. The plasmoids across multiple z - x planes constitute the *fibers* in the *pancake*. With the progress of CMR, the *fibers* (also the entire *pancake*) gradually converge to the middle symmetric axis (the y -axis in our coordinate system). At $t=5$

Myr, the single main (~ 20 pc) *filament* forms along the axis. The maximum density reaches $n_{\text{H,tot}} \sim 10^9 \text{ cm}^{-3}$, while the typical density is $n_{\text{H,tot}} \gtrsim 2 \times 10^3 \text{ cm}^{-3}$. At two ends of the *filament*, there are *forks* that are reminiscent of those structures at both ends of the Orion A cloud and the California cloud (see Figure 6 of Lada et al. 2009). Around the main *filament*, there is a lower density “halo” with $n_{\text{H,tot}} \lesssim 2 \times 10^3 \text{ cm}^{-3}$ (for $t \gtrsim 4$ Myr). This “halo” is the relic of the *pancake*. There are

rich accompanying *fibers* around the “halo” and the *filament*. Combining Figures 3 and 2, we can see that MRCOLA_CNM indeed produces a large filamentary cloud along y-axis. Star formation happens along this *filament*. Note, the length scale of the *filament* is about 10 times larger than that from K22, which is inline with the scale increase of the simulation.

Figure 5 provides a better view of the plasmoids and the squeezing of the *pancake*. Here we show slice plots of $y=0$ plane, so we see the cross-section of the *pancake* and the *filament*. We can see *field-loops* forming around the *pancake* (with sharp turning points at $z \sim \pm 7$ pc). Inside the *field-loop*, there are multiple over-dense spots along the *pancake*. The spots are cross-sections of the *fibers* as shown in Figure 3. The *field-loop* formation is due to magnetic reconnection at two ends of the *pancake* and the spots are follow-up over-densities due to the plasmoid instability at the field-reversal interface. Again, see K21 for a detailed description (e.g., their Figures 24, 25). The reconnected *field-loops* continuously squeeze the *pancake* to the central axis. Consequently, from $t=3$ Myr, we see the accumulation of gas into the main *filament*. Throughout the collision, *field-loops* continuously transport dense gas to the main *filament*. Simultaneously, star formation happens along the *filament* length, showing a dynamic star formation picture.

3.3. Molecular Gas Formation

A major goal of this paper is to test whether a molecular cloud can form through CMR. The first quantity we examine is the molecular gas fraction $[H_2] \equiv n_{H_2}/n_{H,tot}$. If all H atoms are in molecular form, i.e., the *filament* is fully molecular, the molecular fraction $[H_2]$ should be 50%. If the *filament* is fully atomic, $[H_2]$ should be simply 0. From previous sections we have seen that CMR gradually creates the *filament*. Here we examine its molecular fraction as a function of time.

Figure 6 shows the time-dependent $[H_2]$ from our fiducial model MRCOLA_CNM. Initially, $[H_2]$ is simply zero because the model started with all H in atomic form. At $t=2$ Myr, we begin to notice an elevated $[H_2]$ in the central *pancake*. We have seen the dense *pancake* in §3.1 and Figure 3. There the *pancake* developed *fibers*. Here, similar *fibers* are also visible in $[H_2]$, indicating an ongoing molecular formation. With the progress of the simulation, $[H_2]$ elevates in the *fibers* which merge into the central main *filament*. The two ends of the main *filament* also show the *fork* morphology. Sink formation happens along the *filament* near the central part. At $t=5$ Myr, a single *filament* with $[H_2]$ approaching 0.5 (fully molecular) is present with sinks in the middle. By this time, the total molecular mass is $\sim 800 M_\odot$.

While the density plot showed a “halo” around the center of the *filament* (Figure 3, §3.1), the molecular enhancement in the $[H_2]$ plot is more like a pure *filament* because the density “halo” is not dense enough to produce a large amount of molecular gas. Regardless, Figure 6 shows that CMR of CNM indeed creates a giant molecular cloud (~ 20 pc).

A molecular cloud is typically observed in CO and its isotopologues. So in Figure 7 we show the CO abundance $[CO] \equiv n_{CO}/n_{H,tot}$ development as a function of time. Our chemical module is based on Gong et al. (2017). Although they used a simplified chemical network, their $[CO]$ agreed well with the more sophisticated PDR code (Tielens & Hollenbach 1985). Our implementation includes several additional reactions that make the network more robust when dealing with hot, shocked gas. Full details of these modifications can be found in Hunter et al. (2023). The H_2 formation in Gong et al. (2017) is robust in the sense that it agrees with Tielens & Hollenbach (1985); Nelson & Langer (1999).

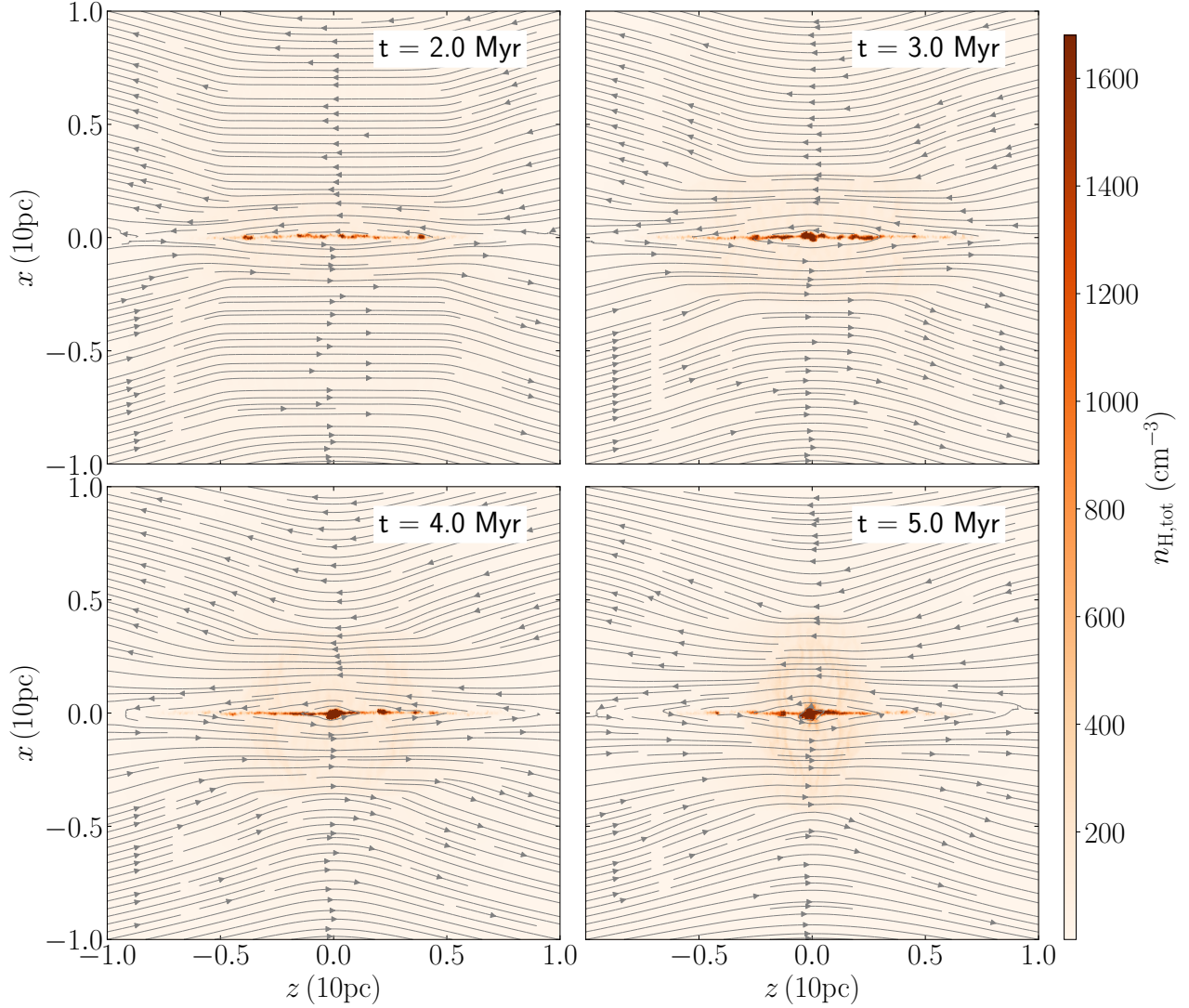


Figure 5. MRCOLA_CNM density slice plots for the $y=0$ plane (compared to Figure 1b). The linear color scale shows the total gas density in unit of $n_{\text{H,tot}}$. The vector stream lines show the field lines in the plane. Note how the reconnected lines encircles the high-density *pancake* at $x=0$. The time step is shown at the top-right. This slice corresponds to Figure 1(b).

In MRCOLA_CNM, initially all Carbon is in C^+ and there is no CO. Following Glover et al. (2010), we adopt an initial elemental abundance for carbon as 1.4×10^{-4} and for oxygen as 3.2×10^{-4} (Sembach et al. 2000). Oxygen is all in atomic form which is subsequently tracked by conservation laws of abundance and charge (Gong et al. 2017).

As shown in Figure 7, [CO] is marginally noticeable at $t=2$ Myr when the maximum [CO] reaches $\sim 6.9 \times 10^{-8}$ and the maximum den-

sity $n_{\text{H,tot}} \sim 9.2 \times 10^3 \text{ cm}^{-3}$. With the progress of the simulation, dense *fibers* build up and merge into the main *filament*. The morphology of [CO] enhancements follows the density and $[\text{H}_2]$ enhancements. The morphological match indicates that H_2 and CO formation quickly follows the accumulation of dense gas because the chemical timescale is relatively short, which is consistent with the findings in Glover et al. (2010) who used a more sophisticated chemical network and started with a condition simi-

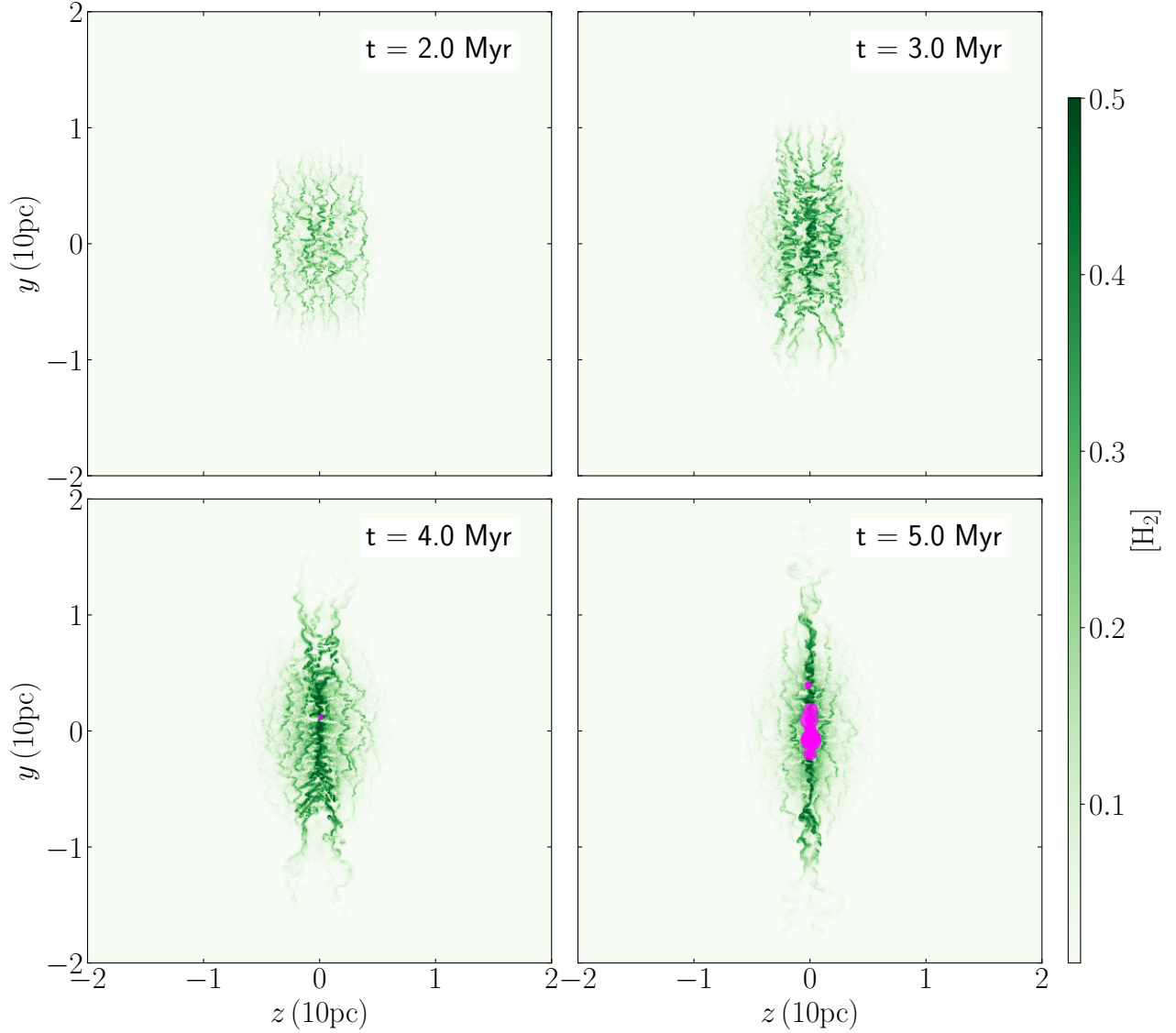


Figure 6. MRCOLA-CNM molecular fraction $[H_2]$ slice plots for the collision mid-plane ($x=0$). This is the same slice as Figure 3. The linear color scale shows $[H_2]$ from 0 to 0.5 (fully molecular). The magenta filled circles show the sinks. The circle size is proportional to the sink mass. The time step is shown at the top-right.

lar to CNM. Finally at $t=5$ Myr, the $[CO]$ enhancement appears as a single *filament* without the “halo”, simply because the “halo” is not dense enough compared to the *filament*. The *filament* and its immediate surroundings have $[CO] \gtrsim 10^{-8}$, with innermost clumps having $[CO] \sim 1.4 \times 10^{-4}$, i.e., all carbon in CO ¹. These results confirm the earlier $[H_2]$ result that

CMR creates a single filamentary giant molecular cloud with a fully molecular spine. Again, our findings show that a molecular cloud can emerge from a CNM gas collision between reverse magnetic fields, as long as the condition allows CMR to produce enough dense gas.

3.4. Synthetic observations

3.4.1. Dust emission

¹ Note that CO depletion is not included.

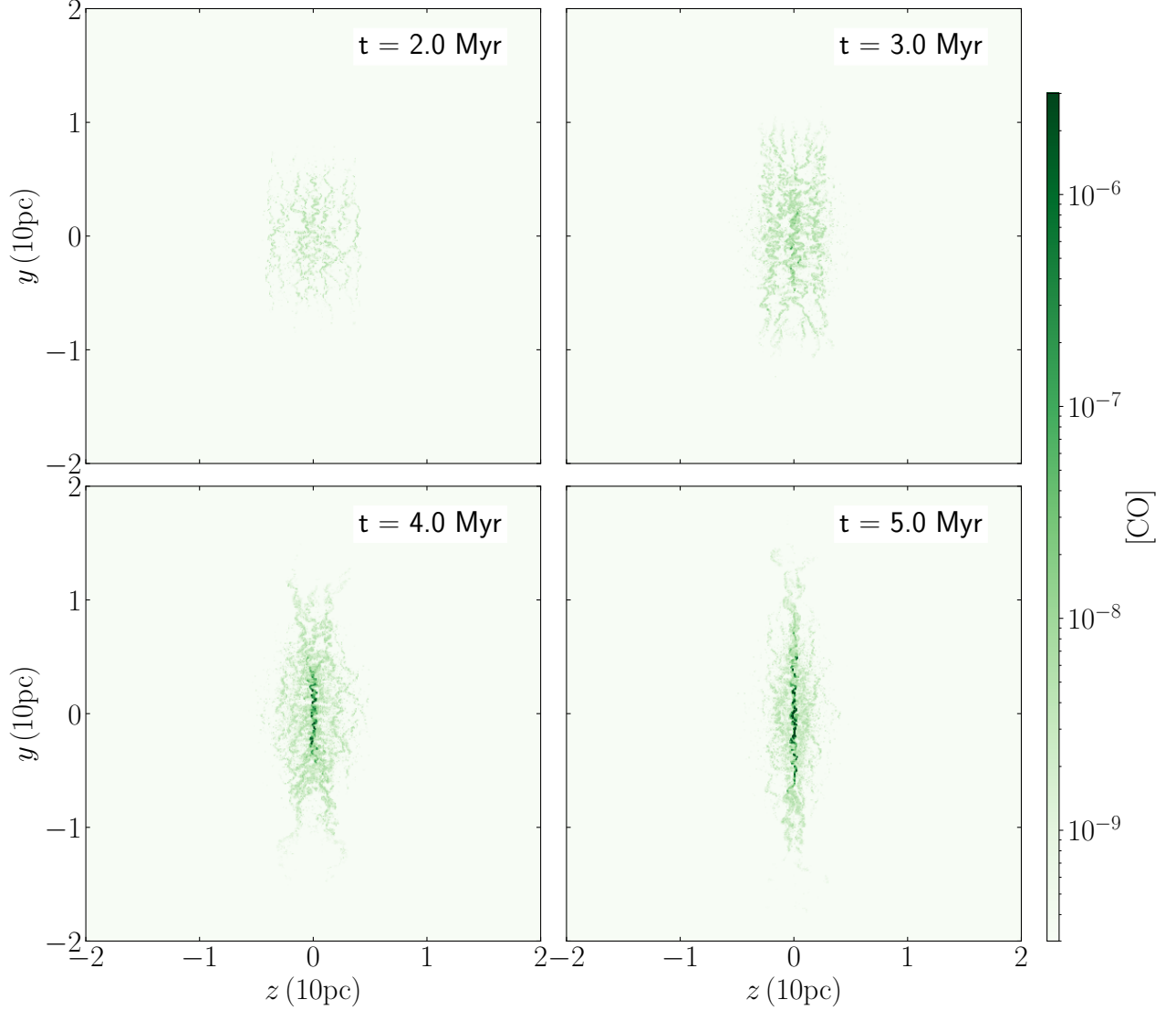


Figure 7. MRCOLA_CNМ molecular abundance [CO] slice plots for the collision mid-plane ($x=0$). This is the same slice as Figure 3. The logarithmic color scale shows [CO] from 3×10^{-10} to 3×10^{-6} . The time step is shown at the top-right.

To show the dust emission at far infrared wavelengths, we carry out radiative transfer (RT) modeling of the *filament*. We use the RT code RADMC-3D (Dullemond 2012) for this purpose. The standard dust-to-gas mass ratio of 0.01 is adopted. The dust is modeled with an amorphous spherical silicate grain with radius $0.1 \mu\text{m}$. The opacity at $250 \mu\text{m}$ is a factor of 4 smaller than the thin ice mantle model from Ossenkopf & Henning (1994) in which dust evolution was considered. So our dust emission, if optically thin, could be underestimated by the

factor if there was grain growth. In our simulation, the majority of the dust has a temperature of $\sim 16 \text{ K}$ because it is in equilibrium with the ISRF. In the spine of the *filament*, the dust temperature is as low as $\sim 5 \text{ K}$ due to the high extinction. Figure 8 shows the $250 \mu\text{m}$ emission for different viewing angles. The pixel scale is 0.02 pc and no beam convolution is applied. Nor do we add any noise.

As shown in Figure 8, the morphology of the dense gas is indeed filamentary, with a length of 10-20 pc depending on the projection. In

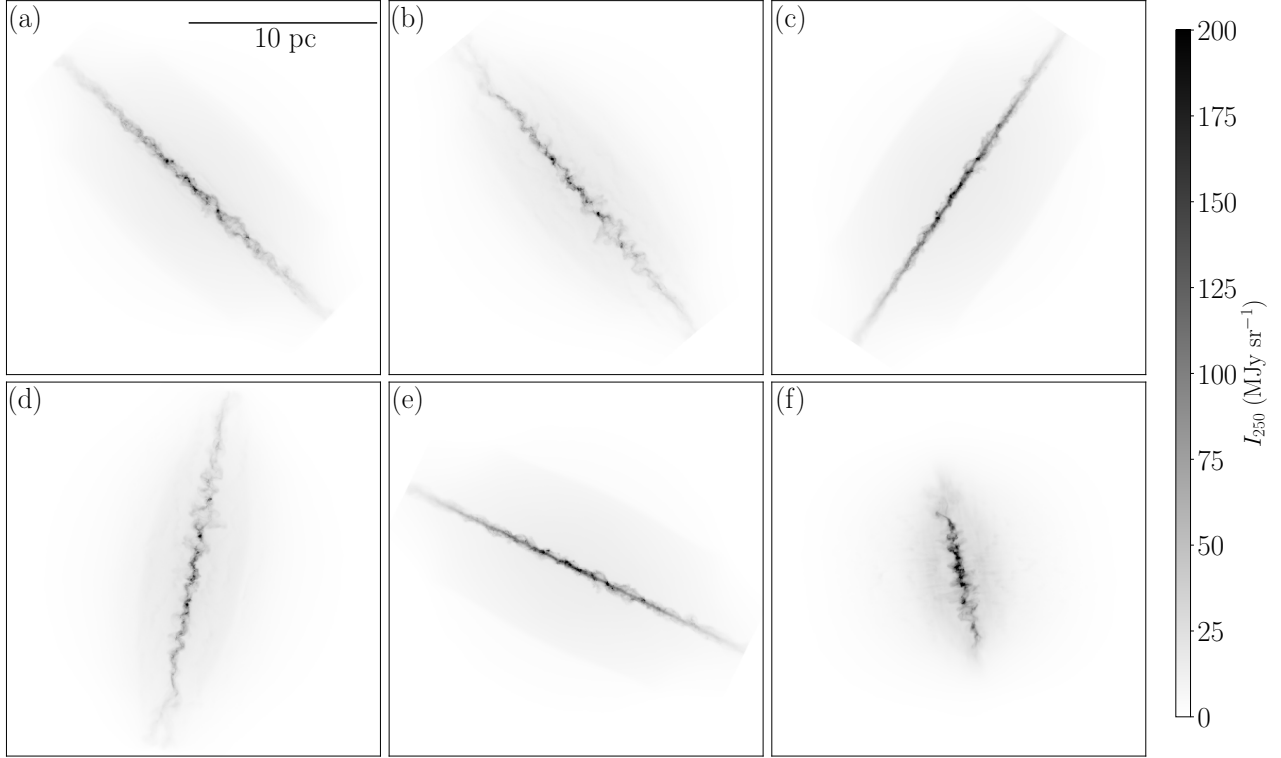


Figure 8. MRCOLA_CNM synthetic observations of dust emission at $250\ \mu\text{m}$ at $t=5\ \text{Myr}$. In each panel we view the entire *filament* ($\sim 20\ \text{pc}$) at a random orientation (not a slice plot). The pixel scale is $0.02\ \text{pc}$, corresponding to $10''$ at a distance of $400\ \text{pc}$. The color bar has units of MJy sr^{-1} .

all panels, the *filament* shows *fibers*. Panels (a)(c)(e) show *rings* along the *filament*. Panels (b)(d) show a *fork* at one end of the *filament*. Multiple dense cores show up as dark dots in the central portion of the *filament*. In general, the plane-of-sky magnetic fields are perpendicular to the filament, while the line-of-sight fields reverse on two sides of the filament, similar to the scenario in Orion A (Heiles 1997; Soler 2019).

Figure 9 shows a zoom-in view to the central $2\ \text{pc}$ region at $t=5\ \text{Myr}$. Again we use RADMC-3D (Dullemond 2012) to model the $250\ \mu\text{m}$ emission for different projections. We adopt a smaller pixel size of $0.004\ \text{pc}$, corresponding to $2''$ at a distance of $400\ \text{pc}$. To match the resolution in Figure 8, we smooth the image to $10''$. We overplot the sinks in the RT images. Their sizes are proportional to their masses.

As shown in Figure 9, the *fibers* are more prominent in the zoomed view. They show a chaotic organization but constitutes the over-

all filamentary morphology. The *fibers* show up in all projections. The overall *filament* is like a bundle of *fibers* thanks to the cylindrical symmetry of the reconnected helical field. Although we are not reproducing a particular molecular cloud, the morphology and the intensity is reminiscent of the Taurus L1495 filament, which has typical values around $\sim 100\ \text{MJy/sr}$ (Palmeirim et al. 2013). The converging gas flow in the *pancake* (Figure 4 and the movie) potentially explains the mass accretion in the sheet-like gas around the filament (Shimajiri et al. 2019). Note, however, at the small scale of *fibers*, non-ideal MHD effects may be important. For instance, Kong et al. (2023) showed that higher Ohmic resistivity resulted in less *fibers* and a smoother overall morphology. It is also not clear if gas and dust reacts to CMR differently since K21 showed slightly different morphologies between far infrared dust

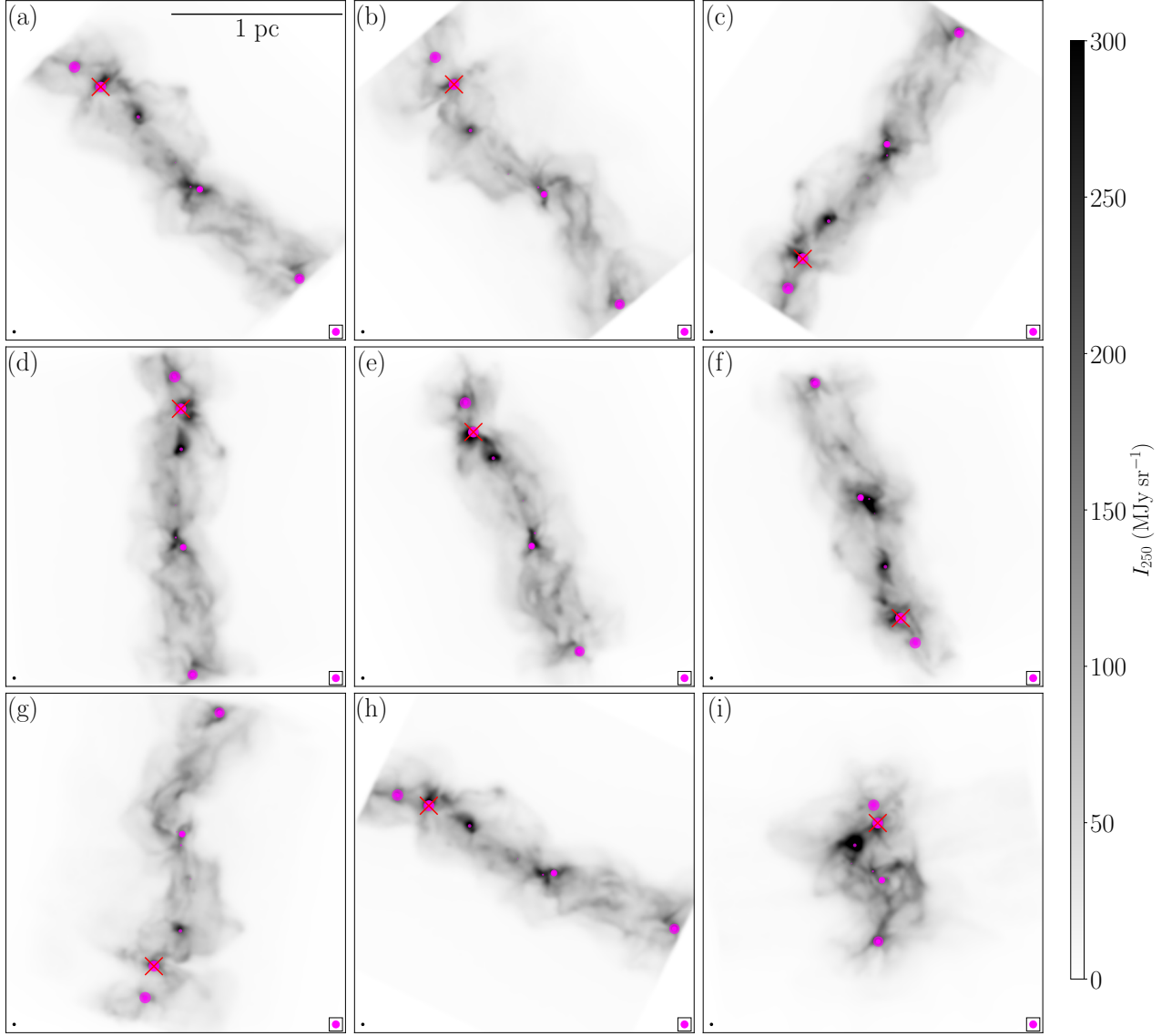


Figure 9. Zoom-in views of the central 2 pc region of the 250 μm emission at $t=5$ Myr. Again each panel shows a random viewing angle of the *filament* (not a slice plot). The images are smoothed to a spatial resolution of $10''$, corresponding to 0.02 pc at a distance of 400 pc. The lower-left black filled circle shows the $10''$ beam. The color bar has units of MJy sr^{-1} . The magenta filled circles are the sinks. Their sizes are proportional to the mass. The red cross marks the location of sink-31. The lower-right legend represents an $8 M_{\odot}$ sink.

emission and molecular line emission (C^{18}O) in the Stick-filament.

At the intersection of the *fibers*, gas may become self-gravitating and collapse, thus we see dense cores develop with connecting *fibers* stretching out. Sinks form in the dense cores, suggesting that they are capable of forming new stars. For instance, the sink at the top-left cor-

ner in panel (a) shows a dusty tail. The sink next to it in the same panel shows multiple connecting *fibers*. In fact, there are five sinks at this location, with the most massive one (hereafter sink-31) having $15 M_{\odot}$ (marked with the red cross). In all other panels, sink-31 shows multiple connecting dusty *fibers*. Its mass ($>8 M_{\odot}$) shows the potential of massive star forma-

tion (depending on the star formation efficiency which is not modeled here).

3.4.2. Dust polarization

To show the synthetic dust polarization, we utilize the radiative transfer code POLARIS (Reissl et al. 2016). We adopt a dust model with 62.5% oblate silicate grains and 37.5% oblate graphite grains with a power-law size distribution from $0.005 \mu\text{m}$ to $1 \mu\text{m}$ (Mathis et al. 1977). The dust is aligned to magnetic fields via the radiative torque (RAT) mechanism (Draine & Weingartner 1997; Lazarian & Hoang 2007). Note, the dust model with POLARIS is different from what we adopt for the RADMC-3D model. Polarization would be enhanced if we were to increase the fraction of silicate grains. Since we are showing general features of CMR-filaments and not reproducing specific clouds, we keep both dust models without resolving the inconsistency.

Figure 10 shows the dust polarization at $214 \mu\text{m}$ from the POLARIS modeling. We first show the overall field orientation relative to the *filament* in the left panel. One can see that the field is perpendicular to the *filament*. This result is not surprising as the initial field symmetry determines the *filament* formation, i.e., a CMR-filament must form along the direction that is perpendicular to the initial antiparallel field (see Figure 1). Observationally, this implies that we shall see the plane-of-sky field perpendicular to a CMR-filament if the latter is perpendicular to our line-of-sight. This scenario is consistent with the observations in the Orion A integral-shaped filament (ISF, Bally et al. 1987; Soler 2019). However, if a CMR-filament is inclined, the relative orientation in the plane-of-sky can be oblique simply because of a geometry effect. If two vectors are perpendicular in 3D, their projected relative orientation in 2D can be any angle between 0 and 180° (e.g., see Stephens et al. 2017; Kong et al. 2019). Interestingly, the part

of Orion A to the south of the ISF shows such an oblique filament-field orientation (Soler 2019).

In the right panel, we zoom in to the central 2 pc region. Again, we see that the *filament* is perpendicular to magnetic fields. Two new features are worth mentioning. First, the field orientation in the *filament* is disrupted. This feature is manifested by the randomized segments inside the *filament*. The disruption is a result of the chaotic nature of the reconnected field as well as the turbulent gas motion due to the magnetic transportation (§3.2 and Figure 4). In line with this physical process, the polarization fraction P_l becomes highly fluctuated, which is the second feature as shown in the color map. In contrast, models without CMR typically show smoother P_l (for example, see Reissl et al. 2021). Therefore, one might distinguish CMR from other mechanisms by characterizing their spatial fluctuation frequencies. We defer this analysis to a future study.

We caution here that the dust polarization in and around a forming molecular cloud is subject to a number of factors, in particular the dust composition and evolution (which is not tracked in our simulation). Observationally, polarization detection is also limited by several factors (e.g., sensitivity, wavelength). So the above polarization synthetic observation is only illustrative. A rigorous comparison of polarization between different models may be useful to observationally distinguish them, which is out of the scope of this paper.

3.4.3. Line emission and kinematics

To show the gas component and the kinematics of the *filament*, we carry out RT modeling of CO(1-0) and show the channel maps in Figure 11. Again, we use the RADMC-3D code. Here, we use the non-LTE method with “linemode=3” (see the RADMC-3D documentation for details). We set H_2 as the collision partner without distinguishing between ortho- and para- H_2 . Depending on the density,

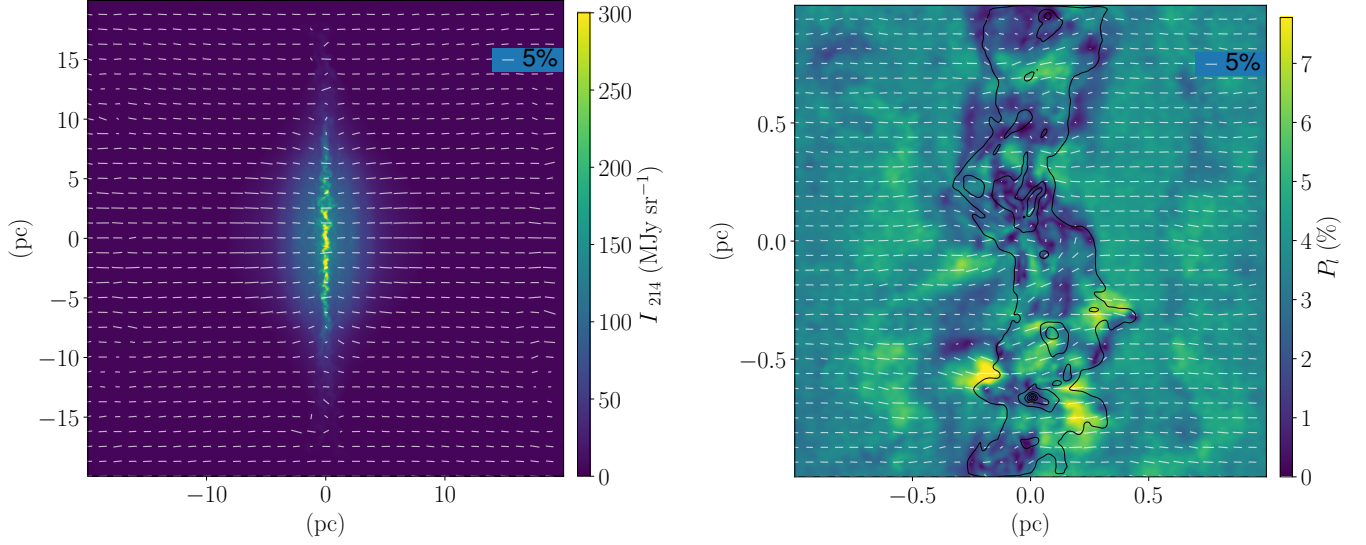


Figure 10. **Left:** Linear polarization P_l overlaid on the Stokes I intensity at $214 \mu\text{m}$. The white segments are oriented along the plane-of-sky fields. Their lengths are proportional to P_l (5% P_l labeled at the top-right). The line-of-sight follows Figure 1(a) except that the cube is rotated by 30° about the y-axis. **Right:** A zoom-in model of the left panel. The color map shows P_l . The black contours show the Stokes I intensity. The map has a beam size of $10''$.

the temperature, and the linewidth, a CO column density of 10^{17} cm^{-2} is marginally optically thick in CO(1-0), with an optical depth $\tau \sim 2$. In the simulation domain, more than 99% of the area has a column density below 10^{17} cm^{-2} . Therefore, the majority of the domain is still optically thin, except for several dense clumps in the *filament*. So the channel maps should show the true internal structures of the *filament* for the most part. The highest CO column density reaches $3.3 \times 10^{20} \text{ cm}^{-2}$. Modern millimeter telescopes with advanced spectrometers can typically reach a spectral resolution of 0.05 km s^{-1} , which we adopt for our line cube. We also match the spatial resolution to Figure 9.

As shown in Figure 11, for the majority of the CO gas, CO(1-0) emission shows a span of about 1 km s^{-1} , except for gas around sinks which shows higher velocities. Since we set up the fiducial model MRCOLA.CNM as a head-on collision, the *filament* is at a stagnation point, thus the limited velocity range in line emission. An off-axis collision (e.g., K21 and K22) should result in a rotation of the *filament*, thus a wider

velocity span. Still, there are multiple velocity components in the channel maps. Here, the general morphology of the CO emission appears to be turbulent with rich sub-structures, mostly *fibers* and clumps. Several *fibers* and clumps are clearly coherent, e.g., the *fiber* in the middle of the first row and the two *fibers* in the middle and the bottom of the second row. The rich sub-structures over multiple velocities are consistent with the aforementioned supersonic turbulence.

In Figure 13(a), we show the CO(1-0) spectrum at a location without sinks. The location is marked as the plus sign in Figure 11. The spectrum shows double velocity components with a velocity separation $\sim 1 \text{ km s}^{-1}$. To compare this with the sound speed, we plot a histogram of CO-dominated gas temperatures in Figure 12. The CO-domination is defined as CO abundance greater than half the initial elemental abundance of Carbon (see §3.3). We can see the CO-dominated gas has a temperature ranging from 5 K to 35 K, with a peak around 11 K. The peak temperature corresponds to a sound speed of $\sim 0.2 \text{ km s}^{-1}$. Therefore, the

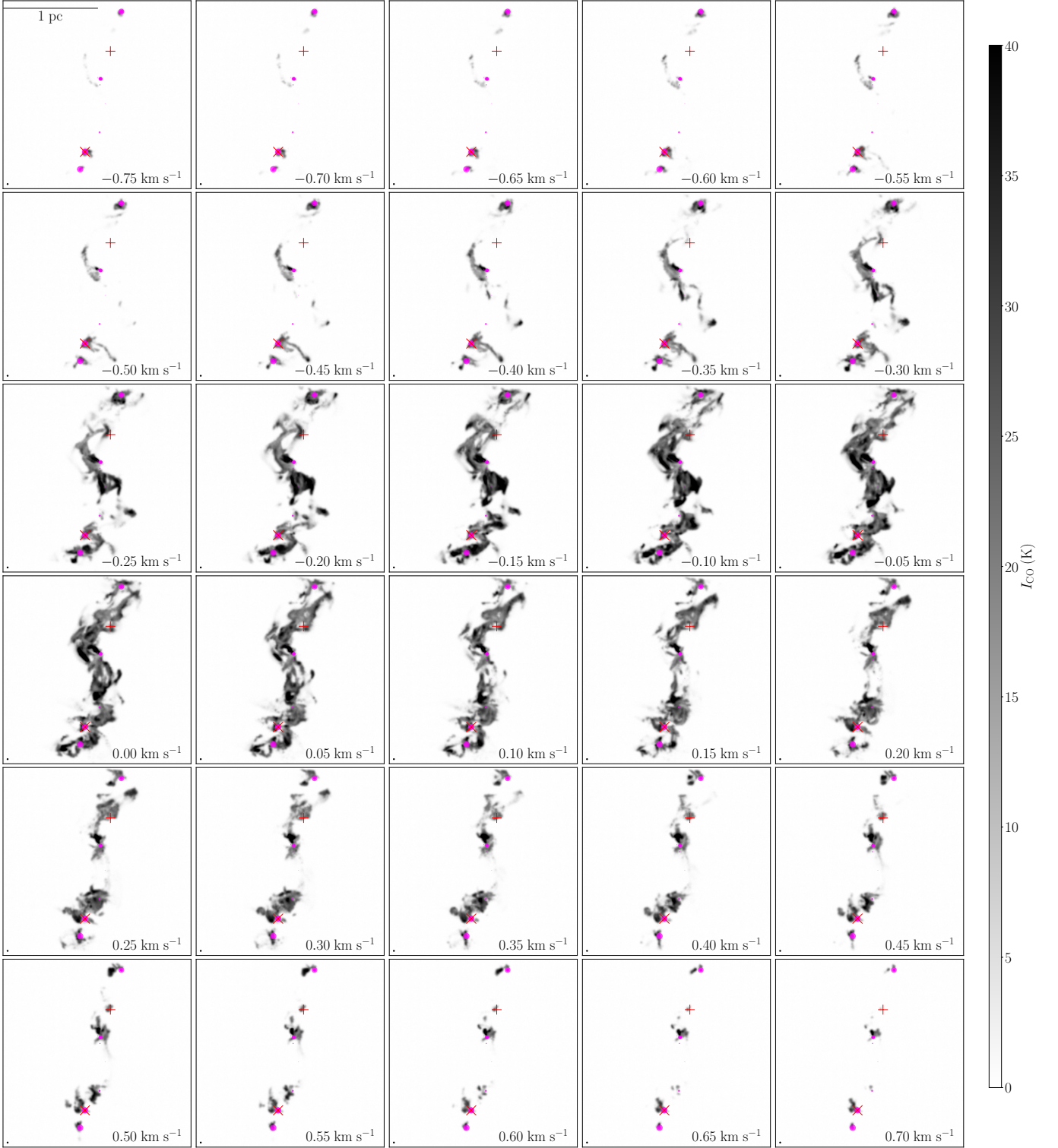


Figure 11. CO(1-0) channel maps from RT modeling of Figure 9(g). The color scale shows the emission intensity in K. To match Figure 9, the channel maps are smoothed to a Gaussian beam with a FWHM of $10''$, which is shown at the lower-left corner in each panel. The channel width is 0.05 km s^{-1} , and the channel velocity is shown at the lower-right corner. The magenta filled circles are the same as those in Figure 9(g). The red cross marks the location of sink-31. The red plus marks the location of no-sink-1.

CO-dominated molecular gas shows supersonic

turbulence. It is also consistent with what we found in §3.2 and Figure 11.

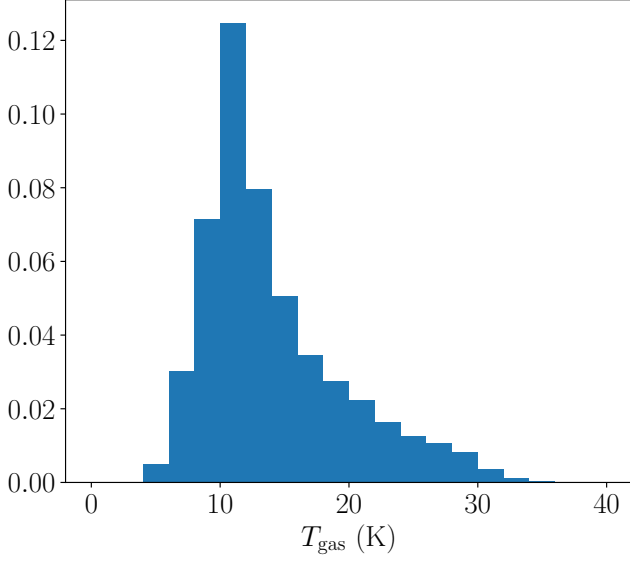


Figure 12. CO-dominated gas temperature histogram in K. The CO-domination is defined as CO abundance greater than half the initial elemental abundance of Carbon.

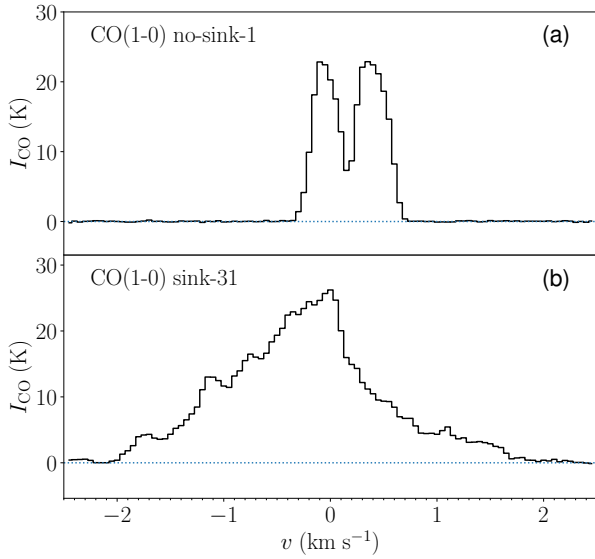


Figure 13. CO(1-0) spectra at two locations (with and without a sink) in Figure 11. The spectral cube is from the RT in §3.4. (a): CO(1-0) spectrum within a $10''$ beam centered at no-sink-1. (b): CO(1-0) spectrum within a $10''$ beam centered at sink-31.

The sinks form in dense gas and some of them are associated with high velocity gas, which is indicative of the active accretion onto the

sink particle. For example, sink-31 in Figure 11 (with the dusty *fibers* as in Figure 9) consistently shows associating gas across all channels, particularly in high-velocity channels. Figure 13(b) shows the CO(1-0) spectrum averaged over a $10''$ beam at sink-31. It shows a non-Gaussian profile with high-velocity tails. The highest velocity reaches 2 km s^{-1} . With a mass of $15 M_{\odot}$, sink-31 has an escape velocity of 5.3 km s^{-1} at the sink creation radius of 0.005 pc . Therefore, the sink is actively accreting material. Note, the gas temperature around sink-31 is $\sim 20 \text{ K}$, corresponding to a sound speed of $\sim 0.3 \text{ km s}^{-1}$.

Combining the above analyses, the overall velocity distribution in the *filament* is a combination of the CMR-induced kinematics and local gravitational infall. Notably, the sink accretion is through streamers. As shown in K22, the streaming accretion is due to the helical field that hinders spherical gas inflow, which limits the accretion rate (and thus the star formation rate), as compared to the same cloud collision but without CMR.

3.5. Models without CMR

Similar to K22, we run two control models with the same cloud collision but without inducing CMR. First, we set up model MRCOLA_CNM_sameB in which the initial magnetic field is uniform. The field strength is the same as MRCOLA_CNM but the field vector points toward positive- z throughout the computational domain. Everything else is the same as MRCOLA_CNM. Table 1 column (3) lists the initial conditions for MRCOLA_CNM_sameB. We run the model up to 11 Myr and see no sink formation. The maximum density briefly reaches $n_{\text{H,tot}} = 10^4 \text{ cm}^{-3}$ at 6.4 Myr but ends up reducing to $\sim 10^3 \text{ cm}^{-3}$ at 11 Myr. The lack of dense gas is not unexpected because the dimensionless mass-to-flux ratio $\mu \equiv (\bar{\Sigma}/B)(2\pi\sqrt{G})$ (Strittmatter 1966; Nakano & Nakamura 1978) for the CNM cloud

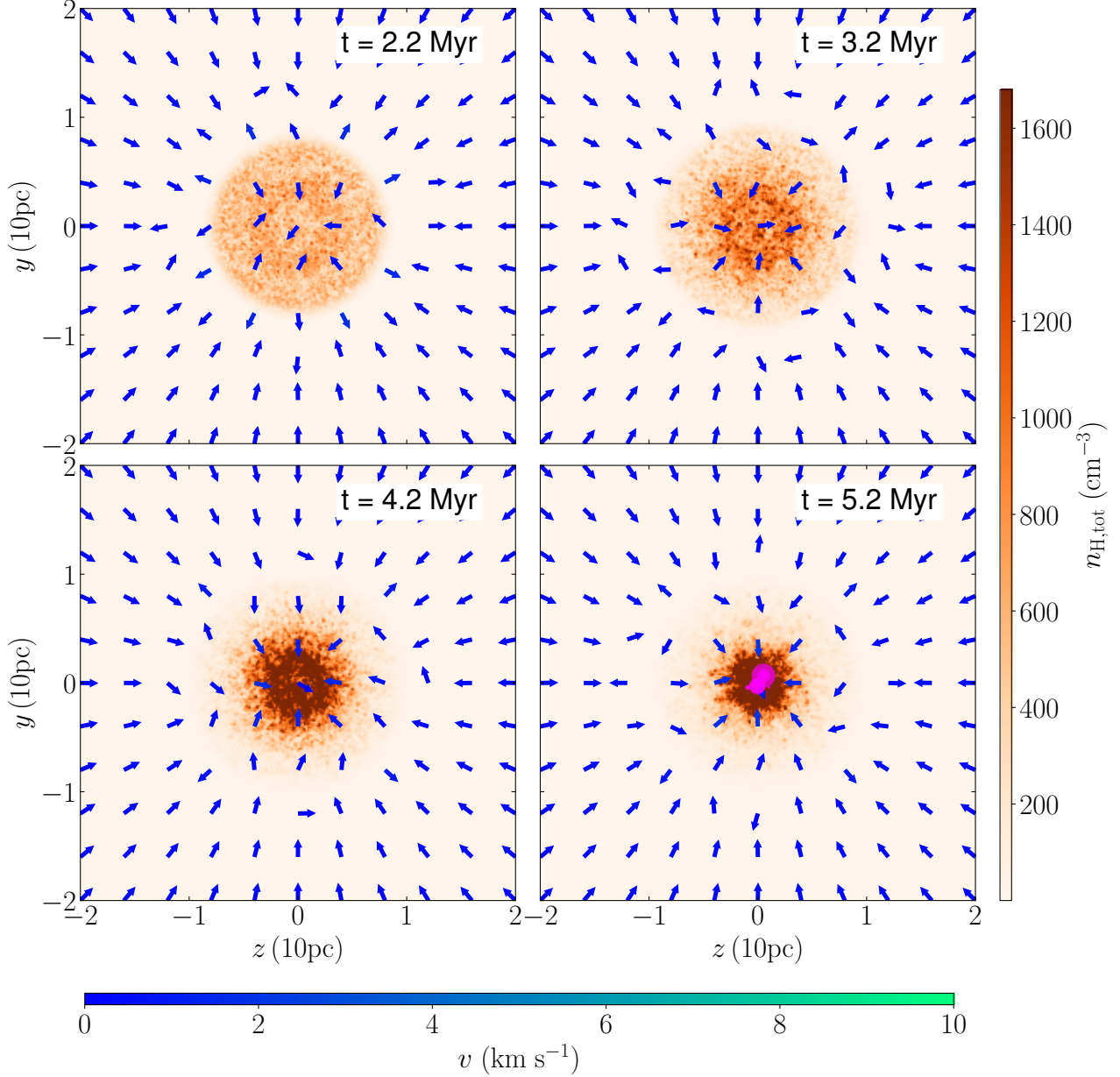


Figure 14. Same format as Figure 3 but for model MRCOLA_CNM_noB.

is ~ 0.85 , i.e., magnetically subcritical. Under such magnetically dominated conditions, dense gas formation is suppressed, and so is star formation. For instance, in a study of cloud-cloud collision, Wu et al. (2020) have shown that star formation is largely suppressed when the cloud transitions from supercritical to subcritical, which is consistent with our results.

Next, we set up MRCOLA_CNM_noB in which we model the cloud collision in purely hy-

drodynamics. Table 1 column (4) lists the initial conditions for MRCOLA_CNM_noB. Besides a zero initial magnetic field strength, we keep everything else the same as MRCOLA_CNM. Figure 14 shows the slice plots for $x=0$ plane from MRCOLA_CNM_noB.

Comparing to MRCOLA_CNM (Figure 3), the collision in MRCOLA_CNM_noB creates a *pancake* which does not become a *filament* throughout the simulation. Starting from $t \sim 3.2$

Myr, the *pancake* collapses symmetrically toward the center, as shown by the velocity vectors. This behavior is expected as the head-on collision has symmetry about the collision axis (x-axis). However, MRCOLA_CNM_noB does not have the cylindrical symmetry along y-axis as MRCOLA_CNM (determined by magnetic fields) therefore there is no *filament* formation. The collapse of the *pancake* gives rise to denser gas at the center of the *pancake*, triggering sink formation at 5.2 Myr (Figure 14 last panel). The sink formation begins somewhat later than MRCOLA_CNM (4 Myr).

The difference shows that the turbulent behavior of CMR produces significant density fluctuations which allows for early dense gas and star formation. On the contrary, star formation in MRCOLA_CNM_noB has to wait for density accumulation through a gradual, ordered collapse. Interestingly, K22 found the opposite at a smaller scale and a higher initial gas density. They showed that the collision between denser molecular clumps formed stars early in the model without magnetic fields. The transition from CNM to molecular gas probably plays a role, which shall be further investigated in detail in the future. In addition, K22 did not model a head-on collision. Nevertheless, neither does MRCOLA_CNM_noB create the *fibers* in the *pancake* (Figure 3), nor does it form a main *filament* as MRCOLA_CNM.

4. DISCUSSION

4.1. Comparison to K22

In this sub-section, we compare our fiducial model MRCOLA_CNM with the fiducial model of K22 MRCOLA. K22 investigated CMR at a factor of 10 smaller scale. At ~ 2 Myr, their *filament* collapsed into a dense core with a cluster of sinks that kept accreting through streamers. In our case, the sinks also develop the streaming accretion. However, the gas dynamics in our case are different from K22. There is no obvi-

ous sign of a global collapse in the *filament* up to the ending of the simulation at 5 Myr. The sinks form at local dense cores that spread out over the main *filament* (Figure 9). On the contrary, the K22 sink formation was due to the longitudinal collapse of the *filament*. The collapse resulted in a dense core in the middle of the *filament* and sinks formed in the dense core (see K22 Figure 2). Their sinks concentrated in the small volume of the dense core (~ 0.1 pc, see K22 Figure 7), unlike in our case the sinks spread over ~ 5 pc.

K22 modeled CMR with an order of magnitude higher initial gas density with a fully molecular chemical condition. So it is understandable that gravity dominated in the K22 *filament* faster than our case. As shown in K22 Figure 2, their *filament* also developed substructures with local density enhancements. It was possible that sink formation could have happened in those enhancements if their *filament* did not collapse. In our model, the global *filament* collapse does not have a chance to develop yet while a few of the sinks are already $> 8 M_{\odot}$. Thanks to the complex dynamics induced by CMR, dense cores are able to form at the intersection of dense *fibers*, allowing the formation of stars without waiting for hierarchical fragmentation to kick in. In fact, due to CMR, the *filament* is never a smooth cylinder even at its formation. So the embedded star formation is not a step-by-step process, i.e., first reaching an equilibrium before developing instabilities which lead to local collapse and star formation. At least with the one model in this paper (MRCOLA_CNM), the whole process of *filament* and star formation is dynamic.

4.2. Timescale of the molecular cloud

Sink formation in MRCOLA_CNM happens around 4 Myr after the CNM cloud collision. However, the *filament* spine is primarily molecular by the 4 Myr mark. The molecular gas fraction is high well before the sink forms (e.g.,

Figure 6). On the other hand, even at 5 Myr, there are only 57 sinks in MRCOLA_CNM, 5 of which with a mass $>8 M_{\odot}$. However, the Orion A giant molecular cloud has thousands of young stars (if not more) with a typical age of 1-2 Myr (e.g., Hillenbrand 1997; Fang et al. 2021). If Orion A formed via CMR as we suspected, then there could be a long, quiescent phase of the molecular cloud prior to the active star formation. Alternatively, the collision could have been between higher mass clouds that were already at least partially molecular though maybe CO-dark. Note, the timescale under discussion is the cloud age before major star formation, so the cluster age is not relevant.

In fact, the freefall timescale of a typical CNM spherical cloud with $n_{\text{H,tot}} \sim 30 \text{ cm}^{-3}$ is ~ 8 Myr. The contraction of a self-gravitating cloud is slow initially but accelerates later. Depending on the definition of the starting point, the typical starless phase of a contracting cloud should be a few Myr. For example, Vázquez-Semadeni et al. (2019) showed that the time interval between the global contraction of CNM and the initial low-mass star formation was several Myr. Alternatively, if we consider the conversion of HI to H_2 , the timescale is $\tau_{\text{HI} \rightarrow \text{H}_2} \sim 10^3/n_{\text{HI}}$ Myr, assuming an H_2 formation rate coefficient of $\sim 10^{-17} \text{ cm}^3 \text{ s}^{-1}$. Again, adopting our CNM density of $n_{\text{H,tot}} \sim 30 \text{ cm}^{-3}$, the H_2 formation timescale is ~ 30 Myr. Of course, as the cloud collision and CMR progress, the density of the *filament* increases with time. In our fiducial model, the timescale for the starless phase is about 4 Myr. Observationally, the HI-to- H_2 conversion time has been used to estimate the age of molecular clouds. For instance, Goldsmith & Li (2005) studied the HI narrow self-absorption (HINSA, Li & Goldsmith 2003) in several molecular clouds and found that the clouds had ages of 3-10 Myr (or even longer). Their assumption of the physical model was that a sudden density enhance-

ment increased the extinction and greatly reduced photodissociation of H_2 . The enhancement triggered the atomic to molecular transition thus the formation of the molecular cloud. This physical picture is consistent with a cloud-cloud collision scenario, including the CMR cloud formation model in this paper. Following the same methodology, Tang et al. (2020) surveyed HINSA in more clouds and found similar timescales.

Given the above consideration, the long starless phase of the CMR-filament in MRCOLA_CNM is not unexpected. In comparison, the model without CMR has an even longer starless phase of 5 Myr (MRCOLA_CNM_noB, Figure 14). Such a long starless phase is also seen in the colliding flow simulations of Clark et al. (2012b). Their slow collision model, which is more relevant to MRCOLA_CNM_noB (except that MRCOLA_CNM_noB has no seeding turbulence), has a ~ 10 Myr time interval between the cold gas formation and star formation. This phase of the cloud corresponds to the dark molecular gas phase (e.g., Wolfire et al. 2010), which is also present in the CMR-filament.

However, if the simulation begins with a higher initial density, the timescale is much shortened. To show this effect, we run a new simulation with the initial cloud density and magnetic fields a factor of 4 higher than the fiducial model, i.e., $n_1 = n_2 = 120 \text{ cm}^{-3}$ and $B_{1,z} = -B_{2,z} = 20 \mu\text{G}$. These conditions are similar to those adopted in Wu et al. (2020). We terminate the simulation at $t=2$ Myr. Hereafter, we name this new model MRCOLA_CNM4.

Figure 15 shows the [CO] for the new model. Compared to the fiducial model (Figure 7), MRCOLA_CNM4 forms the *filament* a factor of $\gtrsim 2$ times faster. So the starless phase is much shorter. Moreover, the amount of molecular gas in MRCOLA_CNM4 is much larger than MRCOLA_CNM. Figure 16 shows the compar-

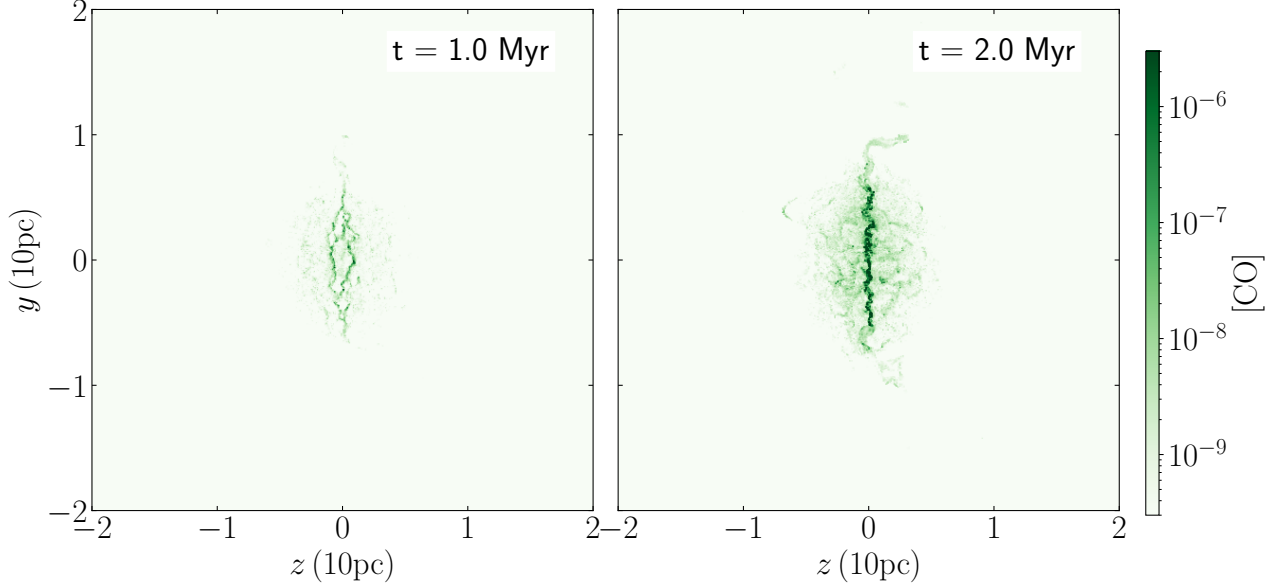


Figure 15. Same format as Figure 7 but for model MRCOLA_CNM4 (see §4.2).

ison. One can see the CO dominated gas in MRCOLA_CNM4 is four times more than the fiducial model, which is not unexpected because the simulation at large scales is scalable. In fact, our choices of the initial density (30 cm^{-3}) and magnetic field strength ($5 \mu\text{G}$) for the fiducial model are challenging for dense gas formation. Our fiducial model proves that CMR is capable of forming molecular clouds with a low initial density. More exploration is necessary to further manifest the capability. For example, higher collision velocity produces denser gas in filament formation (e.g., Abe et al. 2021; Kong et al. 2023). Note, as mentioned in §3.5, the density and field strength do not allow dense gas formation if the field is not antiparallel. The presence of reverse fields overcome the difficulty, highlighting an important capability of CMR.

4.3. Star formation in the CMR-filament

Since we do not consider stellar feedback in our simulations, we stop the fiducial model simulation at 5 Myr when there are five sinks with a mass greater than $8 M_{\odot}$. These massive sinks suggest that massive star formation is possible. The massive stars would impose strong radiative feedback on the CMR-filament, which

would change the subsequent cloud evolution. Massive star formation in CMR-filaments can be an interesting subject to follow up. Additionally, protostellar outflows should also impact the *filament* (e.g. Arce et al. 2010; Nakamura et al. 2011; Kuiper et al. 2016; Offner & Chaban 2017). Therefore, the discussion here about star formation in MRCOLA_CNM is in the sense of the early-stage star formation in CMR-filament.

As we can see in Figures 2 and 3, there is no global (longitudinal) collapse of the CMR-filament through the end of the simulation at 5 Myr. Instead, the velocity arrows show that every part of the *filament* has inflowing gas. However, star formation is already happening in the middle part of the *filament* from $t=4$ Myr. By $t=5$ Myr, new sinks occupy a spatial span of ~ 5 pc region along the *filament*, with the possibility of a few massive stars. These results suggest that at least in MRCOLA_CNM, dense core and star formation does not need a global cloud collapse along the long axis of the *filament*. Instead the stars form within the embedded clumpy dense structures in the *filament*. The *filament* is never a smooth cylinder throughout the sim-

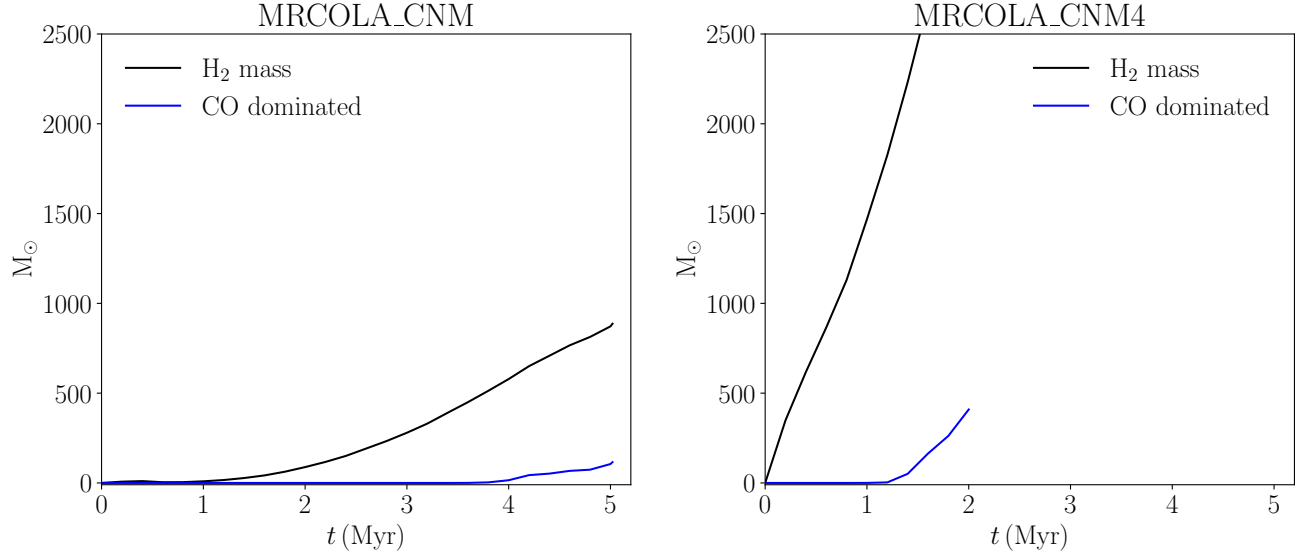


Figure 16. Time-dependent molecular gas mass comparison between MRCOLA_CNM (*left*) and MRCOLA_CNM4 (*right*). The black curve shows the H_2 mass while the blue curve shows the CO dominated gas mass. The two plots have the same x-range and y-range.

ulation, but is instead an ensemble of the dense pieces created by the numerous magnetic reconnection events. The pieces are pulled together to form a *filament* due to the *field-loop* around the *pancake* (Figure 1). The whole *filament* and star formation process is almost a reverse of the canonical cloud and star formation process in which a giant cloud first forms and subsequently fragments into dense cores which possibly form new stars. In the CMR scenario, the dense cores are not fragments of a precursor of smooth *filament* but those dense pieces from supersonic magnetic transportation that later become gravitationally unstable. Another example of bottom-up filamentary cloud formation is from Smith et al. (2016) but the physical forces are different (one hydro+gravity while the other magnetic).

Because star formation happens before global collapse in MRCOLA_CNM, the young stars are not found in a large cluster, although locally there are signs of multiple stars in high column density regions. As shown in §3.4 and Figure 9, the new stars scatter over along the densest parts without obvious signs of clustering. However, it is possible that later the *filament* would

develop large-scale collapse. A (mini) starburst would happen near the collapsing center, qualitatively similar to the cluster formation in K22. On the other hand, a higher initial density may result in a much denser *filament* (Kong et al. 2023) which may develop a global collapse earlier. In reality, gravitational collapse within a large filamentary cloud is observed. For instance, the Orion A cloud (with reverse magnetic fields as in Heiles 1997) is a nice analogy to our CMR-filament in MRCOLA_CNM. Hacar et al. (2017) found evidence of a collapse toward the OMC-1 region in Orion A using position-velocity diagrams (also see Kong et al. 2018; González Lobos & Stutz 2019). The active star formation in ONC (Hillenbrand 1997) could be fed by such collapse.

Regarding Orion A, we can think of its formation history the opposite way. If Orion A were to form via a collision event but with a uniform initial magnetic field, our control model MRCOLA_CNM_sameB showed that it is not possible due to the subcritical mass-to-flux ratio, unless the initial conditions are significantly different. The field strength was based on Zeeman measurements from Heiles (1997), so there

is probably not much leeway for the initial field magnitude. The initial atomic gas density could be much larger than the typical CNM density. Alternatively, a faster colliding speed could also increase the dense gas production in principle, but still the magnetic field should somehow dissipate faster. If the initial collision was parallel to the field, then the magnetic field should not be a problem for dense gas formation. But it would not form a *filament* or explain the reverse field on two sides of the Orion A. CMR provides a compelling case for putting together all observational pieces of a giant filamentary molecular cloud, most importantly including the reverse magnetic field. Because a CMR-filament naturally has a helical field, we would see reverse fields on its two sides regardless of the viewing angle.

5. SUMMARY AND CONCLUSION

In this paper, we have explored the possibility of molecular cloud formation through the Collision-induced Magnetic Reconnection (CMR) mechanism in the cold neutral medium (CNM). Utilizing the AREPO code, we have simulated the collision between two spherical CNM clouds in an environment of warm neutral medium (WNM). The head-on collision happened at the interface of a reverse magnetic field. Similar to previous studies of CMR with molecular gas, the collision between atomic clouds triggered the CMR process. A giant filamentary cloud formed in the collision mid-plane, with rich, fiber-like sub-structures across the entire 20 pc length. In contrast the hydrodynamic reference model formed a flattened *pancake* like cloud, and the MHD case with aligned fields did not form a molecular cloud at all. By the end of the fiducial model simulation at 5 Myr, the CMR *filament* established a fully molecular (H_2) spine, with CO abundances ranging from $\gtrsim 10^{-8}$ to $\sim 10^{-4}$. Starting from 4 Myr, sinks emerged in the middle part of the giant *filament*. By 5 Myr, a total of 57 sinks

formed over a range of ~ 5 pc along the *filament*, 5 of which having a mass greater than $8 M_\odot$ (most massive one reaching $16 M_\odot$). These results suggest that CMR with CNM is capable of forming a giant filamentary molecular cloud with (massive) star formation. CMR provides a compelling case for explaining the formation of giant filamentary molecular clouds with reverse magnetic fields (e.g., Orion A). In this case, magnetic fields play an active, decisive role in the *filament* formation, which is different from previous ideas that the field only has a passive role. Since CMR naturally results in a helical field around the *filament*, we should observe reverse magnetic fields on two sides of the *filament* regardless of the viewing angle.

Synthetic observations of dust emission at far infrared wavelengths revealed numerous dense cores along the CMR-filament. A zoom-in view of the far infrared emission showed that many of the cores host sinks. Some of the cores have more than one sinks. The sinks are typically located at the highest column density part of the core, which typically has multiple connecting *fibers* stretching out. The core-fiber structure implies that the embedded sink is accreting through streamers, consistent with the findings from K22. Contrary to K22 in which the scale was a factor of 10 smaller, the sink formation in this paper is scattered over the central 5 pc length of the *filament* without obvious signs of clustering. The lack of clustering is probably due to the fact that the *filament* shows no sign of a global longitudinal collapse (yet).

The underlying logic is that CMR cloud formation does not follow the canonical top-down picture in which a giant cloud forms first and later fragments into dense cores that make stars. The CMR-filament is clumpy since the beginning because reconnected *field-loops* bring dense gas to the main *filament* piece by piece. These merging dense pieces are created by shocks due to the supersonic magnetic transporta-

tion. They later become gravitationally unstable and form dense cores and stars. So the CMR-filament does not need a global collapse to produce many dense cores and stars, which reflects the chaotic nature of magnetic reconnection. However, we do speculate that large-scale collapse along the *filament* to happen later with possible star cluster formation.

CO(1-0) line emission shows again rich substructures in channel maps, suggestive of turbulence in the CMR-filament. Since the collision is head-on, the span of the velocity range reflects the gas movement along the reconnection interface which is perpendicular to the collision velocity. Due to the pulling of *field-loops*, dense gas in the *pancake* moves toward the central axis with supersonic velocities (sonic Mach number 6-10). Therefore, the filamentary molecular cloud formed via CMR naturally has supersonic turbulence, and the turbulence has a magnetic origin. CMR is thus capable of converting the coherent large-scale motion to small-scale turbulent motion during the formation of the *filament*. Sinks are typically associated with high-velocity gas in CO(1-0) channel maps, indicating active accretion toward the sinks. As long as the collision persists, the CMR process should continuously replenish the *filament* with

turbulence and transfer material to the actively accreting stars, showing a dynamic picture of cloud and star formation.

ACKNOWLEDGMENTS

We thank an anonymous referee for providing constructive reports. SK acknowledges fruitful discussion with Duo Xu, Huabai Li, Stefan Reissl, Serena Kim, and Yancy Shirley. An allocation of computer time from the UA Research Computing High Performance Computing (HPC) at the University of Arizona is gratefully acknowledged. RJS gratefully acknowledges an STFC Ernest Rutherford fellowship (grant ST/N00485X/1) and HPC from the Durham DiRAC supercomputing facility (grants ST/P002293/1, ST/R002371/1, ST/S002502/1, and ST/R000832/1). DJW acknowledges support from the Programa de Becas Posdoctorales of the Dirección General de Asuntos del Personal Académico of the Universidad Nacional Autónoma de México (DGAPA, UNAM, Mexico)

Software: Astropy (Astropy Collaboration et al. 2013), Numpy (van der Walt et al. 2011), Matplotlib (Hunter 2007), SAOImageDS9 (Joye & Mandel 2003)

Facility: UA HPC;

REFERENCES

- Abe, D., Inoue, T., Inutsuka, S.-i., & Matsumoto, T. 2021, ApJ, 916, 83, doi: [10.3847/1538-4357/ac07a1](https://doi.org/10.3847/1538-4357/ac07a1)
- Arce, H. G., Borkin, M. A., Goodman, A. A., Pineda, J. E., & Halle, M. W. 2010, ApJ, 715, 1170, doi: [10.1088/0004-637X/715/2/1170](https://doi.org/10.1088/0004-637X/715/2/1170)
- Astropy Collaboration, Robitaille, T. P., Tollerud, E. J., et al. 2013, A&A, 558, A33, doi: [10.1051/0004-6361/201322068](https://doi.org/10.1051/0004-6361/201322068)
- Bally, J., Langer, W. D., Stark, A. A., & Wilson, R. W. 1987, ApJL, 312, L45, doi: [10.1086/184817](https://doi.org/10.1086/184817)
- Bate, M. R., Bonnell, I. A., & Price, N. M. 1995, MNRAS, 277, 362
- Bhattacharjee, A., Huang, Y.-M., Yang, H., & Rogers, B. 2009, Physics of Plasmas, 16, 112102, doi: [10.1063/1.3264103](https://doi.org/10.1063/1.3264103)
- Burkert, A., & Hartmann, L. 2004, ApJ, 616, 288, doi: [10.1086/424895](https://doi.org/10.1086/424895)
- Chevance, M., Krumholz, M. R., McLeod, A. F., et al. 2023, in Astronomical Society of the Pacific Conference Series, Vol. 534, Protostars and Planets VII, ed. S. Inutsuka, Y. Aikawa, T. Muto, K. Tomida, & M. Tamura, 1, doi: [10.48550/arXiv.2203.09570](https://doi.org/10.48550/arXiv.2203.09570)
- Clark, P. C., Glover, S. C. O., & Klessen, R. S. 2012a, MNRAS, 420, 745

- Clark, P. C., Glover, S. C. O., Klessen, R. S., & Bonnell, I. A. 2012b, *MNRAS*, 424, 2599, doi: [10.1111/j.1365-2966.2012.21259.x](https://doi.org/10.1111/j.1365-2966.2012.21259.x)
- Clark, P. C., Glover, S. C. O., Ragan, S. E., & Duarte-Cabral, A. 2019, *MNRAS*, 486, 4622
- Draine, B. T., & Weingartner, J. C. 1997, *ApJ*, 480, 633, doi: [10.1086/304008](https://doi.org/10.1086/304008)
- Dullemond, C. P. 2012, RADMC-3D: A multi-purpose radiative transfer tool, Astrophysics Source Code Library. <http://ascl.net/1202.015>
- Fang, M., Kim, J. S., Pascucci, I., & Apai, D. 2021, *ApJ*, 908, 49, doi: [10.3847/1538-4357/abcec8](https://doi.org/10.3847/1538-4357/abcec8)
- Fiege, J. D., & Pudritz, R. E. 2000, *MNRAS*, 311, 85, doi: [10.1046/j.1365-8711.2000.03066.x](https://doi.org/10.1046/j.1365-8711.2000.03066.x)
- Glover, S. C. O., Federrath, C., Mac Low, M. M., & Klessen, R. S. 2010, *MNRAS*, 404, 2, doi: [10.1111/j.1365-2966.2009.15718.x](https://doi.org/10.1111/j.1365-2966.2009.15718.x)
- Goldsmith, P. F., & Li, D. 2005, *ApJ*, 622, 938, doi: [10.1086/428032](https://doi.org/10.1086/428032)
- Gong, M., Ostriker, E. C., & Wolfire, M. G. 2017, *ApJ*, 843, 38
- González Lobos, V., & Stutz, A. M. 2019, *MNRAS*, 489, 4771, doi: [10.1093/mnras/stz2512](https://doi.org/10.1093/mnras/stz2512)
- Greif, T., Springel, V., White, S., et al. 2011, *ApJ*, 737, 75
- Großschedl, J. E., Alves, J., Meingast, S., et al. 2018, *A&A*, 619, A106, doi: [10.1051/0004-6361/201833901](https://doi.org/10.1051/0004-6361/201833901)
- Hacar, A., Alves, J., Tafalla, M., & Goicoechea, J. R. 2017, *A&A*, 602, L2, doi: [10.1051/0004-6361/201730732](https://doi.org/10.1051/0004-6361/201730732)
- Hacar, A., Clark, S. E., Heitsch, F., et al. 2023, in *Astronomical Society of the Pacific Conference Series*, Vol. 534, *Protostars and Planets VII*, ed. S. Inutsuka, Y. Aikawa, T. Muto, K. Tomida, & M. Tamura, 153, doi: [10.48550/arXiv.2203.09562](https://doi.org/10.48550/arXiv.2203.09562)
- Hacar, A., Tafalla, M., Forbrich, J., et al. 2018, *A&A*, 610, A77, doi: [10.1051/0004-6361/201731894](https://doi.org/10.1051/0004-6361/201731894)
- Han, J. L., Manchester, R. N., van Straten, W., & Demorest, P. 2018, *ApJS*, 234, 11, doi: [10.3847/1538-4365/aa9c45](https://doi.org/10.3847/1538-4365/aa9c45)
- Heiles, C. 1997, *ApJS*, 111, 245, doi: [10.1086/313010](https://doi.org/10.1086/313010)
- Hillenbrand, L. A. 1997, *AJ*, 113, 1733, doi: [10.1086/118389](https://doi.org/10.1086/118389)
- Hunter, G. H., Clark, P. C., Glover, S. C. O., & Klessen, R. S. 2023, *MNRAS*, 519, 4152, doi: [10.1093/mnras/stac3751](https://doi.org/10.1093/mnras/stac3751)
- Hunter, J. D. 2007, *Computing in Science and Engineering*, 9, 90, doi: [10.1109/MCSE.2007.55](https://doi.org/10.1109/MCSE.2007.55)
- Joye, W. A., & Mandel, E. 2003, in *Astronomical Society of the Pacific Conference Series*, Vol. 295, *Astronomical Data Analysis Software and Systems XII*, ed. H. E. Payne, R. I. Jedrzejewski, & R. N. Hook, 489
- Kong, S. 2022, *ApJ*, 933, 40, doi: [10.3847/1538-4357/ac70cd](https://doi.org/10.3847/1538-4357/ac70cd)
- Kong, S., Arce, H. G., Maureira, M. J., et al. 2019, *ApJ*, 874, 104, doi: [10.3847/1538-4357/ab07b9](https://doi.org/10.3847/1538-4357/ab07b9)
- Kong, S., Ossenkopf-Okada, V., Arce, H. G., Klessen, R. S., & Xu, D. 2023, *ApJS*, 265, 58, doi: [10.3847/1538-4365/acbfb0](https://doi.org/10.3847/1538-4365/acbfb0)
- Kong, S., Whitworth, D. J., Smith, R. J., & Hamden, E. T. 2022, *MNRAS*, 517, 4679, doi: [10.1093/mnras/stac2932](https://doi.org/10.1093/mnras/stac2932)
- Kong, S., Arce, H. G., Feddersen, J. R., et al. 2018, *ApJS*, 236, 25, doi: [10.3847/1538-4365/aabafc](https://doi.org/10.3847/1538-4365/aabafc)
- Kong, S., Ossenkopf-Okada, V., Arce, H. G., et al. 2021, *ApJ*, 906, 80, doi: [10.3847/1538-4357/abc687](https://doi.org/10.3847/1538-4357/abc687)
- Kuiper, R., Turner, N. J., & Yorke, H. W. 2016, *ApJ*, 832, 40, doi: [10.3847/0004-637X/832/1/40](https://doi.org/10.3847/0004-637X/832/1/40)
- Lada, C. J., Lombardi, M., & Alves, J. F. 2009, *ApJ*, 703, 52, doi: [10.1088/0004-637X/703/1/52](https://doi.org/10.1088/0004-637X/703/1/52)
- Lazarian, A., & Hoang, T. 2007, *MNRAS*, 378, 910, doi: [10.1111/j.1365-2966.2007.11817.x](https://doi.org/10.1111/j.1365-2966.2007.11817.x)
- Lewis, J. A., Lada, C. J., Bieging, J., et al. 2021, *ApJ*, 908, 76, doi: [10.3847/1538-4357/abc41f](https://doi.org/10.3847/1538-4357/abc41f)
- Li, D., & Goldsmith, P. F. 2003, *ApJ*, 585, 823, doi: [10.1086/346227](https://doi.org/10.1086/346227)
- . 2012, *ApJ*, 756, 12, doi: [10.1088/0004-637X/756/1/12](https://doi.org/10.1088/0004-637X/756/1/12)
- Li, Z.-Y., & Nakamura, F. 2004, *ApJL*, 609, L83, doi: [10.1086/422839](https://doi.org/10.1086/422839)
- Mathis, J. S., Rumpl, W., & Nordsieck, K. H. 1977, *ApJ*, 217, 425, doi: [10.1086/155591](https://doi.org/10.1086/155591)
- Nakamura, F., Kamada, Y., Kamazaki, T., et al. 2011, *ApJ*, 726, 46, doi: [10.1088/0004-637X/726/1/46](https://doi.org/10.1088/0004-637X/726/1/46)
- Nakano, T., & Nakamura, T. 1978, *PASJ*, 30, 671
- Nelson, R. P., & Langer, W. D. 1999, *ApJ*, 524, 923, doi: [10.1086/307823](https://doi.org/10.1086/307823)
- Offner, S. S. R., & Chaban, J. 2017, *ApJ*, 847, 104, doi: [10.3847/1538-4357/aa8996](https://doi.org/10.3847/1538-4357/aa8996)

- Ossenkopf, V., & Henning, T. 1994, *A&A*, 291, 943
- Pakmor, R., Bauer, A., & Springel, V. 2011, *MNRAS*, 418, 1392
- Palmeirim, P., André, P., Kirk, J., et al. 2013, *A&A*, 550, A38, doi: [10.1051/0004-6361/201220500](https://doi.org/10.1051/0004-6361/201220500)
- Poidevin, F., Bastien, P., & Jones, T. J. 2011, *ApJ*, 741, 112, doi: [10.1088/0004-637X/741/2/112](https://doi.org/10.1088/0004-637X/741/2/112)
- Polychroni, D., Schisano, E., Elia, D., et al. 2013, *ApJL*, 777, L33, doi: [10.1088/2041-8205/777/2/L33](https://doi.org/10.1088/2041-8205/777/2/L33)
- Reissl, S., Stutz, A. M., Klessen, R. S., Seifried, D., & Walch, S. 2021, *MNRAS*, 500, 153, doi: [10.1093/mnras/staa3148](https://doi.org/10.1093/mnras/staa3148)
- Reissl, S., Wolf, S., & Brauer, R. 2016, *A&A*, 593, A87, doi: [10.1051/0004-6361/201424930](https://doi.org/10.1051/0004-6361/201424930)
- Sembach, K. R., Howk, J. C., Ryans, R. S. I., & Keenan, F. P. 2000, *ApJ*, 528, 310, doi: [10.1086/308173](https://doi.org/10.1086/308173)
- Shimajiri, Y., André, P., Palmeirim, P., et al. 2019, *A&A*, 623, A16, doi: [10.1051/0004-6361/201834399](https://doi.org/10.1051/0004-6361/201834399)
- Smith, R. J., Glover, S. C. O., Klessen, R. S., & Fuller, G. A. 2016, *MNRAS*, 455, 3640, doi: [10.1093/mnras/stv2559](https://doi.org/10.1093/mnras/stv2559)
- Smith, R. J., Treß, R. G., Sormani, M. C., et al. 2020, *MNRAS*, 492, 1594, doi: [10.1093/mnras/stz3328](https://doi.org/10.1093/mnras/stz3328)
- Soler, J. D. 2019, *A&A*, 629, A96, doi: [10.1051/0004-6361/201935779](https://doi.org/10.1051/0004-6361/201935779)
- Soler, J. D., Bracco, A., & Pon, A. 2018, *A&A*, 609, L3, doi: [10.1051/0004-6361/201732203](https://doi.org/10.1051/0004-6361/201732203)
- Springel, V. 2005, *MNRAS*, 364, 1105
- . 2010, *MNRAS*, 401, 791
- Stephens, I. W., Dunham, M. M., Myers, P. C., et al. 2017, *ApJ*, 846, 16, doi: [10.3847/1538-4357/aa8262](https://doi.org/10.3847/1538-4357/aa8262)
- Strittmatter, P. A. 1966, *MNRAS*, 132, 359, doi: [10.1093/mnras/132.2.359](https://doi.org/10.1093/mnras/132.2.359)
- Stutz, A. M., & Kainulainen, J. 2015, *A&A*, 577, L6, doi: [10.1051/0004-6361/201526243](https://doi.org/10.1051/0004-6361/201526243)
- Tahani, M., Plume, R., Brown, J. C., & Kainulainen, J. 2018, *A&A*, 614, A100, doi: [10.1051/0004-6361/201732219](https://doi.org/10.1051/0004-6361/201732219)
- Tahani, M., Plume, R., Brown, J. C., Soler, J. D., & Kainulainen, J. 2019, *A&A*, 632, A68, doi: [10.1051/0004-6361/201936280](https://doi.org/10.1051/0004-6361/201936280)
- Tahani, M., Lupypciw, W., Glover, J., et al. 2022, *A&A*, 660, A97, doi: [10.1051/0004-6361/202141170](https://doi.org/10.1051/0004-6361/202141170)
- Tang, N.-Y., Zuo, P., Li, D., et al. 2020, *Research in Astronomy and Astrophysics*, 20, 077, doi: [10.1088/1674-4527/20/5/77](https://doi.org/10.1088/1674-4527/20/5/77)
- Tielens, A. G. G. M., & Hollenbach, D. 1985, *ApJ*, 291, 722, doi: [10.1086/163111](https://doi.org/10.1086/163111)
- Tress, R. G., Smith, R. J., Sormani, M. C., et al. 2020, *MNRAS*, 492, 2973, doi: [10.1093/mnras/stz3600](https://doi.org/10.1093/mnras/stz3600)
- Truelove, J. K., Klein, R. I., McKee, C. F., et al. 1997, *ApJL*, 489, L179
- van der Walt, S., Colbert, S. C., & Varoquaux, G. 2011, *Computing in Science & Engineering*, 13, 22, doi: [10.1109/MCSE.2011.37](https://doi.org/10.1109/MCSE.2011.37)
- Vázquez-Semadeni, E., Palau, A., Ballesteros-Paredes, J., Gómez, G. C., & Zamora-Avilés, M. 2019, *MNRAS*, 490, 3061, doi: [10.1093/mnras/stz2736](https://doi.org/10.1093/mnras/stz2736)
- Wolfire, M. G., Hollenbach, D., & McKee, C. F. 2010, *ApJ*, 716, 1191, doi: [10.1088/0004-637X/716/2/1191](https://doi.org/10.1088/0004-637X/716/2/1191)
- Wu, B., Tan, J. C., Christie, D., & Nakamura, F. 2020, *ApJ*, 891, 168, doi: [10.3847/1538-4357/ab77b5](https://doi.org/10.3847/1538-4357/ab77b5)
- Zhao, B., Pudritz, R. E., Pillsworth, R., Robinson, H., & Wadsley, J. 2024, *arXiv e-prints*, arXiv:2405.18474, doi: [10.48550/arXiv.2405.18474](https://doi.org/10.48550/arXiv.2405.18474)